High-Coherence Kerr-Cat Qubit in 2D Architecture

Ahmed Hajr,[1,*,†] Bingcheng Qing,[1,*] Ke Wang,[1] Gerwin Koolstra,[1] Zahra Pedramrazi,[1,2] Ziqi Kang,[1] Larry Chen,[1] Long B. Nguyen,[1] Christian Jünger,[1,2] Noah Goss,[1] Irwin Huang,[3] Bibek Bhandari,[4] Nicholas E. Frattini,[5,‡] Shruti Puri,[5] Justin Dressel,[4] Andrew N. Jordan,[3,4,6] David I. Santiago,[2] and Irfan Siddiqi[1,2]

[1]*Quantum Nanoelectronics Laboratory, Department of Physics, University of California at Berkeley, Berkeley, California 94720, USA*
[2]*Computational Research Division, Lawrence Berkeley National Laboratory, Berkeley, California 94720, USA*
[3]*Department of Physics and Astronomy, University of Rochester, Rochester, New York, USA*
[4]*Institute for Quantum Studies, Chapman University, Orange, California, USA*
[5]*Department of Applied Physics and Physics, Yale University, New Haven, Connecticut 06520, USA*
[6]*The Kennedy Chair in Physics, Chapman University, Orange, California 92866, USA*

(Received 3 May 2024; revised 29 August 2024; accepted 11 October 2024; published 20 November 2024)

The Kerr-cat qubit is a bosonic qubit in which multiphoton Schrödinger cat states are stabilized by applying a two-photon drive to an oscillator with a Kerr nonlinearity. The suppressed bit-flip rate with increasing cat size makes this qubit a promising candidate to implement quantum error correction codes tailored for noise-biased qubits. However, achieving strong light-matter interactions necessary for stabilizing and controlling this qubit has traditionally required strong microwave drives that heat the qubit and degrade its performance. In contrast, increasing the coupling to the drive port removes the need for strong drives at the expense of large Purcell decay. By integrating an effective band-block filter on chip, we overcome this trade-off and realize a Kerr-cat qubit in a scalable 2D superconducting circuit with high coherence. This filter provides 30 dB of isolation at the qubit frequency with negligible attenuation at the frequencies required for stabilization and readout. We experimentally demonstrate quantum nondemolition readout fidelity of 99.6% for a cat with eight photons. Also, to have high-fidelity universal control over this qubit, we combine fast Rabi oscillations with a new demonstration of the $X(\pi/2)$ gate through phase modulation of the stabilization drive. Finally, the lifetime in this architecture is examined as a function of the cat size of up to ten photons in the oscillator, achieving a bit-flip time higher than 1 ms and only a linear increase in the phase-flip rate, in good agreement with the theoretical analysis of the circuit. Our qubit shows promise as a building block for fault-tolerant quantum processors with a small footprint.

DOI: 10.1103/PhysRevX.14.041049

Subject Areas: Optics, Quantum Physics, Quantum Information

I. INTRODUCTION

Superconducting quantum circuits offer a rich platform for engineering Hamiltonians that encode and manipulate quantum information faster than the decoherence rates [1–10]. Integrating the Josephson junction into those circuits enables a wide range of nonlinear terms in the Hamiltonian that can be used to implement multiphoton wave mixing processes in the microwave range [11,12].

In particular, the family of cat qubits uses this nonlinearity to stabilize the superposition of macroscopically distinct so-called Schrödinger cat states. Depending on the details of the encoding scheme, those qubits can exhibit either exponential protection or parity changes with single-photon loss, making them a valuable resource for implementing quantum error correction schemes [13–24]. One approach to stabilize those states with autonomous protection from bit flips is by engineering two-photon addition and subtraction in the case of the dissipative cat. This approach offers exponential protection with increasing cat size but requires external ancillas to engineer the dissipation and perform readout [19,25–27].

An alternative approach to stabilize the cat states is by subjecting a Kerr nonlinear oscillator to a coherent two-photon drive [28,29]. This approach has the advantage of

*These authors contributed equally to this work.
†Contact author: hajr@Berkeley.edu
‡Present address: Nord Quantique, Sherbrooke, Quebec J1J 2E2, Canada.

creating a relatively large energy gap (5–100 MHz) between the computational space and the rest of the Hilbert space, enabling fast logic operations (20–400 ns) and high-fidelity readout with no added ancillas. The Kerr-cat qubit gained a lot of attention in terms of examining its noise-biased behavior both theoretically [30–34] and experimentally [20,35–38]. Also, this qubit makes a promising candidate to implement the *XZZX* surface code, provided it can be realized in a scalable architecture [39–41].

The protection against single-photon loss in this qubit can be intuitively understood by noting that the coherent states $|\pm\alpha\rangle$ are quasiorthogonal eigenstates of the annihilation operator ($\hat{a}$) with eigenvalues $\pm\alpha$; with this bosonic enhancement factor, the dominant process of single-photon loss leads only to a linear increase in the qubit dephasing at the benefit of exponential suppression in the relaxation rate. The first realizations of this qubit were in 3D architectures and relied on strong microwave drives which led to notable heating and degraded the qubit lifetime [20,35,38]. Therefore, it is still an open question to see whether it is possible to realize large cat states with high coherence in 2D chips while maintaining high-fidelity operations. This uncertainty arises because the 3D environment is known to result in longer lifetimes but weaker light-matter coupling due to the larger spread of the electromagnetic field in the extra dimension [42–44].

Realizing a 2D circuit with strong light-matter coupling without sacrificing the lifetime is crucial to scaling up the Kerr-cat qubit. The inherent trade-off is that coupling the drive port strongly to the qubit (i.e., large coupling capacitance) leads to large Purcell decay. In contrast, coupling weakly at the expense of strong driving heats the qubit and degrades its performance, as shown in other strongly driven qubits [25,45].

In this work, we overcome this challenge by using an effective band-block filter that enables strong coupling off resonance (at the frequency of the stabilization drive ω_S and the cat readout drive ω_{CQR}) while suppressing the qubit Purcell decay rate orders of magnitude smaller than the limit imposed by materials defects. Operating at a Kerr nonlinearity of 1.2 MHz, we observe improvements in the bit-flip time with increasing drive strength up to a cat of size ten photons. The bit-flip time exceeds 1 ms while increasing the phase-flip rate only linearly with the cat size. Also, the large energy gap at this Kerr value enables us to perform the highest-fidelity readout and gates on Kerr cats to date. Our work, therefore, provides a path for scaling noise-protected qubits toward fault-tolerant quantum computers.

II. ENCODING

The Kerr-cat qubit has the following Hamiltonian in the rotating frame [28,29]:

$$\hat{H}_{KC}/\hbar = -K\hat{a}^{\dagger 2}\hat{a}^2 + \epsilon_2\hat{a}^{\dagger 2} + \epsilon_2^*\hat{a}^2, \tag{1}$$

where K is the strength of the Kerr nonlinearity, ϵ_2 is the amplitude of the two-photon drive (i.e., the stabilization drive), and $\hbar$ is the reduced Planck constant. This Hamiltonian stabilizes two coherent states $|\pm\alpha\rangle$ provided the cat size $\alpha^2 = \epsilon_2/K$. The cat states are the orthogonal even- and odd-parity states formed by the superposition of the coherent states $|C_\alpha^\pm\rangle = (1/\sqrt{1 \pm e^{-2\alpha^2}})(1/\sqrt{2})(|\alpha\rangle \pm |-\alpha\rangle)$ and span the Bloch sphere along the x axis as shown in Fig. 1(a). The orthogonal states along the z axis are approximately the coherent states [i.e., $|\pm Z\rangle = (1/\sqrt{2})(|C_\alpha^+\rangle \pm |C_\alpha^-\rangle) \approx |\pm\alpha\rangle$]. The energy pseudopotential of this Hamiltonian is a double well with an energy gap $E_{gap}/\hbar \approx 4K\alpha^2$ [30] separating the computational space from the rest of the Hilbert space as shown in Fig. 1(b).

This Hamiltonian is now traditionally realized by charge pumping a superconducting nonlinear asymmetric inductive element (SNAIL) oscillator with a coherent drive at approximately twice the oscillator (i.e., qubit) frequency $\omega_S \approx 2\omega_Q$ [20,35]. Utilizing the third-order nonlinearity of the SNAIL $\hat{\varphi}^3$ (where $\hat{\varphi}$ is the superconducting phase operator), a photon from the drive is consumed to create two photons in the oscillator ($a^{\dagger 2}$) at the rate ϵ_2; this is accompanied by the complementary process of eliminating two photons from the oscillator ($\hat{a}^2$) and creating a pump photon [46–48]. The other nonlinearity of the SNAIL is fourth order ($\hat{\varphi}^4$), which in the rotating wave approximation (RWA) adds the Kerr nonlinearity $-K\hat{a}^{\dagger 2}\hat{a}^2$ to the Hamiltonian. We refer to this element in the Fock encoding as the SNAILmon (i.e., transmon with small anharmonicity provided by the SNAIL).

III. DESIGN

The 2D superconducting circuit used to realize the Kerr-cat qubit with the SNAILmon is shown in Figs. 1(e)–1(g). The design of the SNAILmon contains two large niobium capacitor paddles and is based on high-coherence transmon qubit designs [49,50]. In addition, our design contains two SNAILs consisting of aluminum Josephson junctions fabricated with a bridge-free two-angle deposition process. Concatenating multiple SNAILs has allowed large cat sizes in previous Kerr-cat qubit experiments [35]. The readout circuitry contains a readout resonator coupled to a Purcell filter (green), which allows for fast readout while protecting the qubit from Purcell decay. For control, a weakly coupled port [c' in Fig. 1(c)] is used for on-resonance driving. For stabilization and readout, a strongly coupled port is used for efficient pumping [c_p in Fig. 1(c)] with an effective band-block filter to suppress the Purcell decay.

The nonlinearities of our circuit can be tuned with an external flux piercing each SNAIL. In this work, we fix the external flux to realize a Kerr nonlinearity of $K/2\pi = 1.2$ MHz, a value between the first realization of the Kerr cat (6.7 MHz) [20], which showed fast control but limited bit-flip protection with increasing cat size

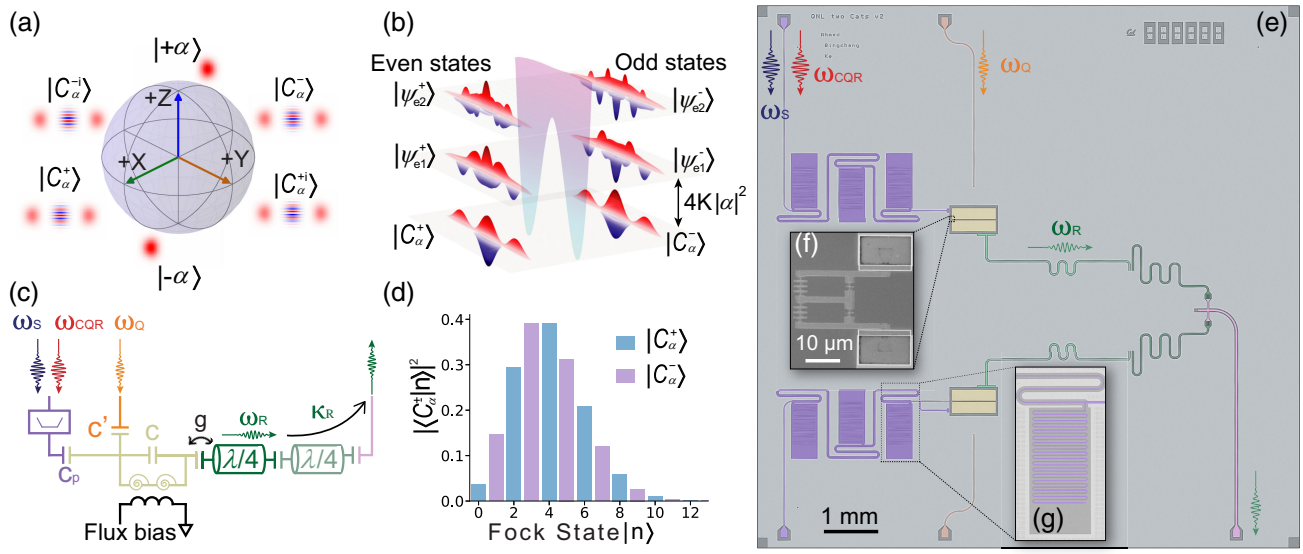

FIG. 1. Kerr-cat qubit encoding and 2D chip architecture. (a) The Bloch sphere for the Kerr-cat qubit is spanned by the cat states along the x axis and the coherent states along the z axis. (b) The energy pseudopotential is a double-well potential at $\pm\alpha$ with energy gap $4K\alpha^2$ separating the computational space from the excited states. The Wigner function of the cat states and the excited states are shown according to the parity. (c) The circuit diagram shows the nonlinear oscillator with the ports used for stabilization (c_p), control (c'), and readout. The numerical values of the design parameters are reported in Table I. (d) The distribution of the cat states with an average photon number equal to 4 (i.e., $|\alpha|^2 = \langle\hat{a}^\dagger\hat{a}\rangle$) in terms of the Fock states showing the parity of the cat states and the tail of the distribution. (e) The 2D chip (10×10 mm^2) includes two uncoupled SNAILmons (yellow), each with its dedicated readout resonator and Purcell filter (light and dark green). Resonant drives at frequency ω_Q are delivered through weakly coupled control lines (orange), while the strong off-resonant drives used for stabilization (ω_S) and cat readout (ω_{CQR}) are delivered through a strongly coupled port with a band-block filter (purple). (f) The nonlinearity of the oscillator comes from two SNAIL loops biased around $\Phi_{ext}/\Phi_0 = 0.3$ by an off-chip flux coil. (g) Each stub of the filter consists of a meander section to have destructive interference around the qubit frequency.

(i.e., number of photons), and the smaller value (0.3 MHz) in Refs. [35,38], which sacrificed the gate speed in favor of increasing bit-flip protection with a larger number of photons. At the chosen operating point for our qubit, we observe an improvement in the bit-flip time by increasing the number of photons to 10 while maintaining the ability to perform fast logic gates and coherent mapping between the Fock qubit and the cat qubit if needed (see Fig. 7 in Appendix D 2).

The band-block filter we use to couple strongly to the stabilization and readout drives is shown in Figs. 1(e) and 1(g). This filter consists of multiple stubs, each leading to destructive interference of the microwave signal around the qubit frequency. This is achieved by adjusting the length of the meandering section (i.e., the quarter wave resonators) and simulating the scattering parameters in Ansys-HFSS [51]. Ideally, this filter has high isolation at the qubit frequency ($\omega_Q/2\pi = 5.9$ GHz) with zero attenuation at the frequency of the stabilization drive ($\omega_S/2\pi = 11.8$ GHz) and the frequency of the cat quadrature readout ($\omega_{CQR}/2\pi = 1.2$ GHz). In Fig. 2, we present an independent measurement of the transmission coefficient $\bar{S}_{21}$ of the filter in a dedicated chip (for more details about the setup, see Appendix G). In Fig. 2(a), we show the behavior of the normalized scattering parameter $\bar{S}_{21}$ for the full range of interest. The 30 dB of isolation at the qubit frequency corresponds to a 3-orders-of-magnitude improvement in the lifetime, pushing the Purcell limit through the strongly coupled port to 12 ms, which is much higher than the measured single-photon decay time of the Fock qubit of $T_1 = 38.5$ μs. Material defects in the interfaces have been shown to limit the lifetime of 2D architectures at this range [52–57].

In Fig. 2(b), we enlarge around the qubit frequency to examine the range of 20 and 30 dB of isolation. The large bandwidth of this filter makes it suitable for multiqubit chips with strong qubit-qubit coupling while maintaining a negligible Purcell effect and efficient pumping for all the qubits. This filter can also be incorporated in any circuit QED experiment in which a strong off-resonance drive is required to implement the desired interaction [58–60]. The idea of integrating on-chip filters to enable strong coupling with mitigated Purcell effects was first introduced in the context of fast readout [12,61,62], and the use of band-block filters to enable strong coupling off resonance was also explored more recently [63,64].

IV. QUBIT CONTROL AND READOUT

To create the Kerr-cat qubit, we ramp up the stabilization drive to transform the SNAILmon Hamiltonian to the

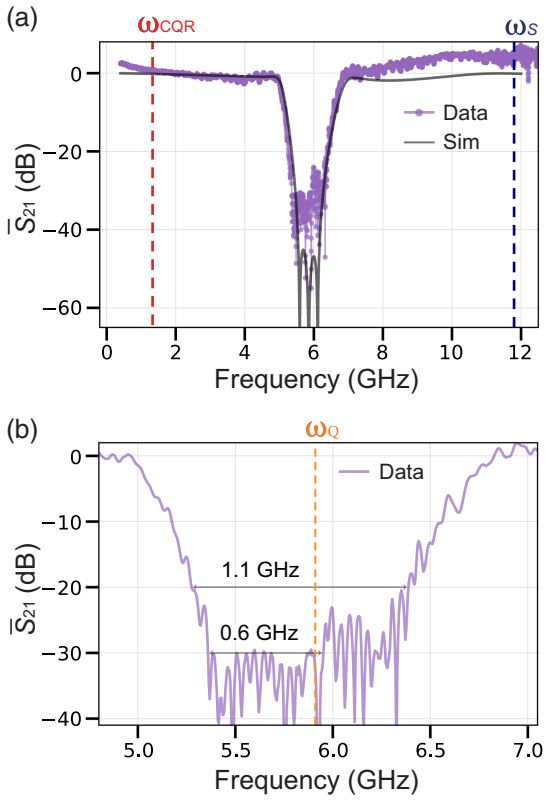

FIG. 2. The transmission parameter of the wide band-block filter used for strong qubit-drive coupling. (a) The measured performance for the full range of the filter (purple). The dark gray line is the simulated performance using finite-element simulation. The filter has minimum attenuation at the frequency of the stabilization drive ω_S and the cat quadrature readout ω_{CQR}. At the qubit frequency ω_Q, the filter provides very high isolation of 30 dB. (b) Enlarged view around the qubit frequency with the 20,30 dB attenuation ranges, which makes this filter suitable for multiqubit chips with strong coupling between the qubits and large detuning due to its large bandwidth.

Kerr-cat qubit Hamiltonian in the rotating frame (see Appendix A for derivation). In this section, we focus on characterizing the readout and the single-qubit gates for a cat of size $\alpha^2 = 4$ (see Appendix D for more details). Starting with the cat quadrature readout in Fig. 3(a), we can measure the qubit along the z axis by sending a microwave pulse to the qubit at frequency $\omega_{CQR}/2\pi = (\omega_R - \omega_S/2)/2\pi = 1.2$ GHz, which implements a beam-splitter interaction between the qubit and readout mode $\hat{H}_{CQR} \approx \epsilon_{CQR}\alpha\hat{Z}(\hat{b} + \hat{b}^\dagger)$ which is derived in Appendix A 2 [20]. The output signal is a coherent state with one of two opposite phases according to the state of the qubit, as shown in Fig. 3(a). For a cat of size 4 and 4 μs readout time, we measure a QNDness $\mathcal{Q} = [p(+\alpha|+\alpha) + p(-\alpha|-\alpha)]/2$ of 98.3%, where $p(+\alpha|+\alpha)$ is the probability that the second measurement gives $|+\alpha\rangle$ consistent with the first measurement result. This high quantum nondemolition (QND) readout enables us to use the measurement to initialize the qubit in the Z basis. For a cat of size 8, the QNDness of the readout increases to 99.6%, as shown in Fig. 7. Those values are equal to the state of the art across all superconducting qubits [35,65,66].

Universal single-qubit control typically requires driving on resonance to do rotations along two orthogonal axes, depending on the phase of the drive [12,28]. However, this protocol in the cat encoding leads to an enhancement factor 2α in the speed of the $Z(\theta)$ rotations and an exponential suppression of the $Y(\theta)$ rotations [20] (for more details, check Appendix D). To overcome this challenge, it is sufficient to use the $Z(\theta)$ rotations with $X(\pi/2)$ gates to have universal control. The first proposal to do an $X(\pi/2)$ gate was demonstrated in Ref. [20] by abruptly turning off the stabilization drive for a period $\pi/2K = 216$ ns. However, this protocol removes the protection the stabilization drive adds to the qubit, and it tends to have worse performance for large cats [35].

To improve on this implementation, we demonstrate a new $X(\pi/2)$ gate by phase modulating the stabilization drive according to $\epsilon_2 \to \epsilon_2 e^{-it\dot{\delta}_d(t)}$. This modulation modifies the double-well potential and allows the coherent states to tunnel. With the appropriate unitary transformation, the phase modulation of the drive adds the following term to the Kerr-cat Hamiltonian:

$$H_d(t) = -\frac{1}{2}[\dot{\delta}_d(t) + t\ddot{\delta}_d(t)]\hat{a}^\dagger\hat{a}. \tag{2}$$

Figure 3(b) shows the expectation value of Pauli Z after implementing two $X(\pi/2)$ pulses as a function of the maximum detuning δ_0 in the phase modulation waveform and the gate time T_g. This gate implementation is resource efficient, since it does not require additional tones and does not disturb the SNAIL parameters compared to a fast dc flux. The coherent tunneling between the states inside the two energy wells using a controlled time-dependent detuning to perform logic gates was first examined theoretically [28,29,67], and the static detuning was shown to improve the lifetime experimentally [35,38]. The simulation of this gate according to Eq. (2) is shown in Fig. 6 (more details in Appendix C 2). From the chevron plot, we choose $T_g = 320$ ns and a detuning $\delta_0/K = -8.2$ for maximum population transfer.

Next, we calibrate the phase of the drive to implement $Z(\theta)$ rotations by driving on resonance. The added term to the Kerr-cat Hamiltonian has the form $\approx 2\alpha|\Omega_z|\cos(\theta_z)\hat{Z} - 2\alpha\Omega_z\sin(\theta_z)e^{-2|\alpha|^2}\hat{Y}$ as long as the drive amplitude Ω_z is small compared to the energy gap $E_{gap}/\hbar$ [20,30]. Figure 3(c) shows the protocol to calibrate the phase of the drive [$\mathrm{Arg}(\Omega_z) = \theta_z$] by leveraging the cat quadrature readout and the $X(\pi/2)$ gate introduced earlier. The second $X(\pi/2)$ gate enables us to measure Rabi oscillations in $\langle Y\rangle$ as we sweep the phase of the Rabi drive θ_z with maximum contrast $|\langle Y\rangle| \approx 0.9$. When using the traditional $X(\pi/2)$

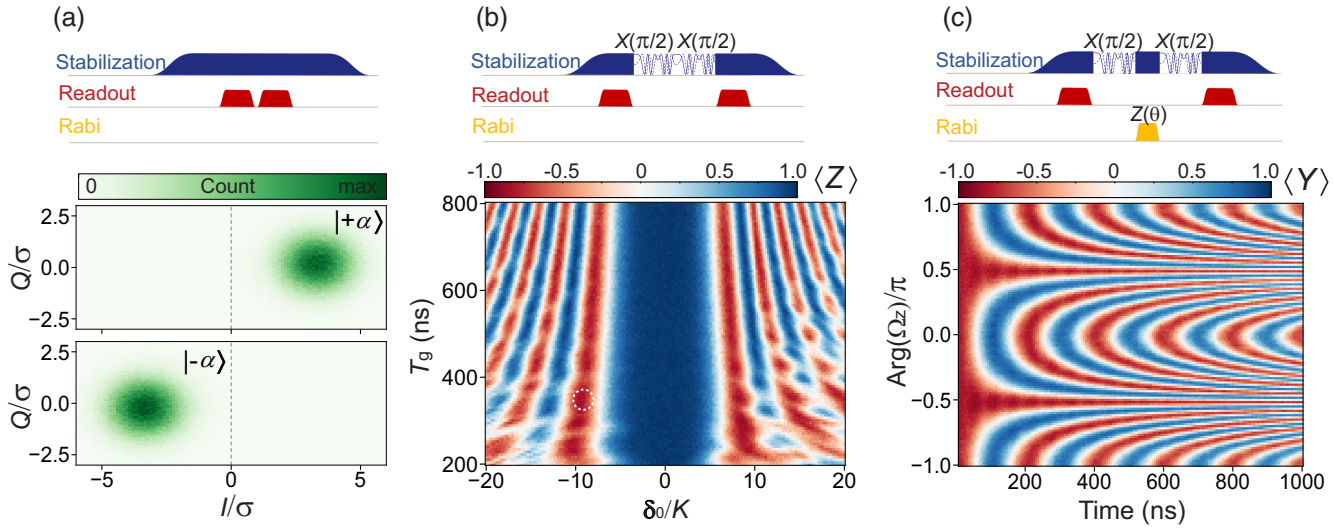

FIG. 3. Readout and gates with the Kerr-cat qubit. (a) The sequence to measure the QNDness of the cat quadrature readout involves two consecutive measurements to determine the probability of getting the same outcome. The demodulated output signal for the second measurement is shown in the IQ plane conditional on the first measurement being $|\pm\alpha\rangle$. The data are normalized with respect to the standard deviation of the Gaussian distribution (σ) of each output. For every initial state, we average 10^7 measurements. (b) The calibration of the detuning $X(\pi/2)$ gate is based on using two $X(\pi/2)$ pulses to flip the qubit and change the sign of $\langle Z\rangle$. This gate is implemented by deforming the double-well potential, allowing the two coherent states to tunnel. The presence of the derivative in Eq. (2) enables one to detune the phase in either direction. The waveform used for the gate in the pulse sequence shows how the two quadratures of the envelope [i.e., intermediate frequency (IF) signal] change to implement the transformation $\epsilon_2 \to \epsilon_2 e^{-it\delta_d(t)}$. The dashed circle indicates the calibration point. (c) The calibration of the drive phase to implement the Z gate is determined by observing the fastest oscillations in $\langle Y\rangle$ (plotted relative to the phase of α). When driving in phase, we get an enhancement factor of 2α, while driving out of phase leads to exponentially suppressed rates.

gate where the stabilization drive is turned off [20], the maximum contrast drops to $|\langle Y\rangle| \approx 0.5$. We can see in Fig. 3(c) that driving in phase leads to the maximum Rabi rate, while driving around $\theta_z = \pm\pi/2$ leads to suppressed rates. For a cat of size 4, we choose a gate time of 120 ns to implement the $Z(\pi/2)$ gate. With the $X(\pi/2)$ and the $Z(\theta)$ calibrated, we have a universal set of single-qubit gates. Using process tomography, we measure gate fidelities $\mathcal{F}_{X_{\pi/2}} = 90.8\%$ and $\mathcal{F}_{Z_{\pi/2}} = 91.7\%$. For the identity, we measure $\mathcal{F}_I = 92.7\%$, which implies that state preparation errors are the limiting factor. The Pauli transfer matrices for those processes with the details of the analysis are provided in Appendix E.

V. CAT QUBIT LIFETIME

We start by measuring the lifetime of the cat qubit as a function of the cat size $\alpha^2 = \epsilon_2/K$ by varying the strength of the two-photon drive ϵ_2 as shown in Fig. 4. Every sequence begins with a readout signal to initialize the qubit in the Z basis. To measure the lifetime of the cat states T_C (i.e., phase-flip time), we use the Kerr $X(\pi/2)$ gate introduced in Ref. [20], since it does not depend on the cat size in the calibration. For every cat size, we vary the delay time Δt to observe the exponential decay of the coherence and perform another $X(\pi/2)$, since the cat readout projects the qubit to the Z basis. The measured lifetime in Fig. 4(a) follows the trend in gray, which is the linear trade-off for large cats described by $T_C = T_1/2\langle\bar{n}\rangle$ with $\langle\bar{n}\rangle = |\alpha|^2(1+e^{-4|\alpha|^2})/(1-e^{-4|\alpha|^2})$ the time-averaged number of photons in the qubit [35].

The linear increase in the phase-flip rate of the cat states should come at the benefit of exponential protection against the single-photon loss in the bit-flip rate. In Fig. 4(b), we examine the lifetime of the coherent states T_α (i.e., bit-flip time) as a function of the cat size. The staircase shape we observe implies that thermal excitations limit the lifetime. A bit-flip error can happen through tunneling to the higher-energy states, which starts to become asymptotically degenerate at the points where the lifetime increases sharply with the cat size. This trend was first observed in Ref. [35]. The staircase behavior is captured by heating effects in the master equation like $\kappa_{\omega_s/2} n_{\omega_s/2} \mathcal{D}\{\hat{a}^\dagger\}$ with $\kappa_{\omega_s/2}$ and $n_{\omega_s/2}$ being the decay rate and thermal population at half stabilization frequency, respectively. The exact location of the plateaus in this model depends on the spectrum of the dephasing noise $\kappa_\phi(\omega)$ [68] (see Appendix B for more details). Our data up to cats of size 8 can be understood in terms of the single- and multiphoton heating and dephasing of the SNAIL with thermal population $n_{\omega_s/2} = 2\%$. This value is the lowest compared to other Kerr-cat experiments or similar strongly driven qubits [45]. However, this is still higher than the upper

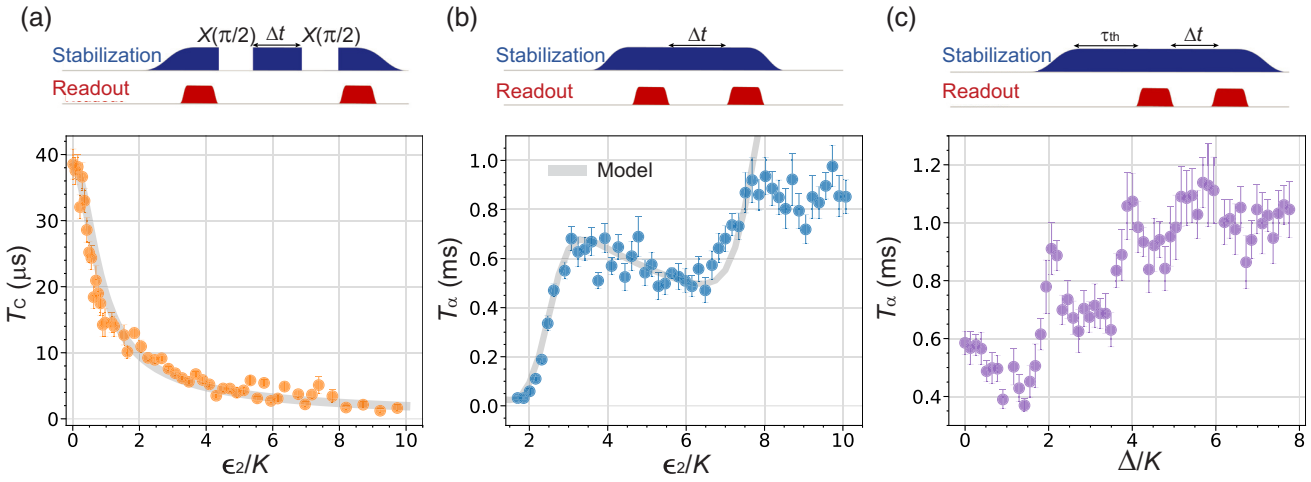

FIG. 4. The lifetime of the Kerr-cat qubit. (a) The sequence to measure the lifetime of the cat states requires ramping up the stabilization drive in $\tau_{\text{ramp}} = 3$ μs to keep the population in the cat space. The first readout is used to initialize the qubit in the Z basis. Two $X(\pi/2)$ gates are used to prepare and measure the lifetime of the cat states T_C (i.e., the phase-flip time) for every cat size $\alpha^2 = \epsilon_2/K$. The lifetime decreases with the cat size, starting with a lifetime of around 38.5 μs, consistent with the single-photon loss being the dominant factor. (b) The lifetime of the coherent states T_α (i.e., bit-flip time) follows a staircaselike behavior with peaks around cat size $\alpha^2 = 3$, 8 and a lifetime of 650 and 950 μs, respectively. The data are fitted to a master equation model, which includes single- and multiphoton heating effects and frequency fluctuations, as explained in the main text and Appendix B. (c) The sequence to prepare the detuned cat includes extra wait time $\tau_{\text{th}} = 35$ μs to put the qubit in a thermal state and use the first readout to prepare the qubit. The data show improvement in the lifetime of the coherent states for a stabilization drive of strength $\epsilon_2/K = 4$, as we introduce a red detuning to the drive in units of the Kerr nonlinearity. The value peaks around even multiples of K due to the acquired degeneracy of the excited states.

bound of 0.3% value we measure from the residual population of the $|n = 1\rangle$ state in the Fock basis [69]. The details of the master equation model are presented in Appendix B.

Next, we focus on cats of size 4, which offer the most gain in T_α without sacrificing T_C much. It is also possible to red tune the stabilization drive to boost the lifetime of the coherent states by adding the harmonic term $\Delta\hat{a}^\dagger\hat{a}$ with $\Delta = \omega_Q - \omega_S/2$ to the Kerr-cat Hamiltonian in Eq. (1) [35,38]. Figure 4(c) shows the improvement in T_α for $\epsilon_2/K = 4$ as we sweep the detuning. The lifetime peaks around even multiples of K due to the Hamiltonian picking extra degeneracies in the excited states [38]. However, in the case of the detuned cat, the ground state of the Fock qubit $|n = 0\rangle$ does not map to the even cat state of the detuned cat qubit, so, instead, we keep the stabilization drive for a time $\tau_{\text{th}} \approx T_1$ necessary to put the detuned cat in a thermal state, and then we use the cat quadrature readout to initialize the qubit. Those results demonstrate the potential of the Kerr-cat qubit to benefit from the suppressed bit-flip rate with only a linear increase in the phase-flip rate with increasing cat size while maintaining high-fidelity operations.

VI. CONCLUSION

Our results demonstrate a high-coherence Kerr-cat qubit in a scalable 2D architecture with high-fidelity single-qubit operations and minimal heating. This demonstration is enabled by integrating a wide band-block filter for efficient energy delivery, enabling strong light-matter coupling with negligible Purcell effect. We report improvement in the bit-flip time up to cats of size $\alpha^2 = 10$ with lifetimes higher than 1 ms, in good agreement with our theoretical modeling of the circuit. Our qubit is based on a SNAILmon oscillator with a single-photon decay time $T_1 = 38.5$ μs.

Operating at a Kerr nonlinearity of 1.2 MHz, we get an energy gap $4K\alpha^2 = 9.6$–48 MHz for cats of size 2–10, which enables fast operation compared to the decay rates. For those device parameters, we demonstrate quantum nondemolition readout with QNDness of 98.3% for a cat of size 4 and 99.6% for a cat of size 8. We also introduce a resource-efficient way to implement the $X(\pi/2)$ gate with phase modulation of the stabilization drive. Combined with continuous and fast $Z(\theta)$ rotations, this is sufficient to have universal control over the Kerr-cat qubit. For a cat of size 4, we implement single qubit $Z(\pi/2)$ in 120 ns and the $X(\pi/2)$ in 320 ns with gate fidelities of 91.7% and 90.8%, respectively, limited by state preparation using process tomography. A detailed analysis of those gates in terms of the noise bias without state preparation and measurement (SPAM) errors is the subject of future work.

With the goal of implementing quantum error correction codes with many physical Kerr-cat qubits, the problem of finding an efficient pumping scheme that does not heat the cryogenic environment is of most importance. Our solution

relies on integrating an effective band-block filter to remove the trade-off between strong capacitive coupling to the qubit and large Purcell decay to enable strong light-matter interactions. With 30 dB of isolation at the qubit frequency, large bandwidth, and negligible attenuation at the pump frequencies, this design enables the realization of multiqubit processors.

In conclusion, we introduced a novel scheme for efficient power delivery in 2D architecture to realize the Kerr-cat qubit with high-coherence, fast logic gates, and state-of-the-art QND readout. This work extends the reach of the Kerr-cat qubit to strongly coupled multiqubit 2D processors, which can be used to examine the fidelity of the noise-bias-preserving two-qubit CZ and CX gates [30] and quantum error correction schemes tailored for noise-biased qubits with Kerr cats [39–41]. Future single-qubit experiments can focus on increasing the Kerr nonlinearity of the qubit without jeopardizing the lifetime to enable faster single-qubit gates with improved fidelity and examine the root causes of the saturation in the lifetime with controlled dissipation.

ACKNOWLEDGMENTS

We thank Chuan-Hong Liu, Akel Hashim, and Ravi Naik for valuable discussions on the experiment. We are grateful to Alexei Marchenkov and Alexander Tselikov for the blueprint of the on-chip rf filter. This work was supported by the U.S. Army Research Office under Grant No. W911NF-22-1-0258.

APPENDIX A: REALIZING THE KERR-CAT HAMILTONIAN FROM THE SNAIL

1. The Kerr-cat Hamiltonian

The Kerr-cat Hamiltonian $\hat{H}_{\mathrm{KC}}$ can be realized by adding a stabilization drive $\hat{H}_S$ at twice the SNAILmon frequency to the SNAIL Hamiltonian ($\hat{H}_a$) and moving to a rotating frame as follows ($\hbar = 1$) [20]:

$$\hat{H}_0 = \hat{H}_a + \hat{H}_S, \tag{A1}$$

$$\hat{H}_a = \omega_{a,0}\hat{a}^\dagger\hat{a} + g_3(\hat{a}^\dagger + \hat{a})^3 + g_4(\hat{a}^\dagger + \hat{a})^4, \tag{A2}$$

$$\hat{H}_S = 2\mathrm{Re}(e^{i\omega_s t})(\epsilon_{s,0}\hat{a}^\dagger + \epsilon^*_{s,0}\hat{a}). \tag{A3}$$

The operator $\hat{a}$ is the bosonic annihilation operator of excitations in the SNAILmon oscillator. The oscillator frequency is $\omega_{a,0}$, and third- and fourth-order nonlinearities are g_3 and g_4, respectively. Now, to eliminate the time dependence, we apply two consecutive transformations. First, we move to a displaced Fock basis characterized by $-\xi_s$ and then to a rotating frame characterized by ω_r:

$$\hat{U} = \hat{U}_{\mathrm{rot}}\hat{U}_{\mathrm{dis}} = e^{i\omega_r t\hat{a}^\dagger\hat{a}} \cdot e^{\xi_s\hat{a}^\dagger - \xi_s^*\hat{a}}. \tag{A4}$$

This leads to the effective Hamiltonian $\hat{H}_{\mathrm{KC}} = \hat{U}\hat{H}_0\hat{U}^\dagger + i\dot{\hat{U}}\hat{U}^\dagger$. The second term in $\hat{H}_{\mathrm{KC}}$ eliminates the harmonic part in $\hat{U}\hat{H}_0\hat{U}^\dagger$ if $\omega_r = \omega_{a,0}$. More precisely,

$$i\dot{\hat{U}}\hat{U}^\dagger = -\omega_r\hat{a}^\dagger\hat{a} + ie^{i\omega_r t\hat{a}^\dagger\hat{a}}(\dot{\xi}_s\hat{a}^\dagger - \dot{\xi}_s^*\hat{a})e^{-i\omega_r t\hat{a}^\dagger\hat{a}}. \tag{A5}$$

The impact of sandwiching $\hat{H}_0$ is summarized by first displacing a ($a^\dagger$) by ξ_s (ξ_s^*) and then adding a time-dependent factor $e^{-i\omega_r t}$ ($e^{i\omega_r t}$), which is crucial when we apply the RWA as follows:

$$\hat{U}_{\mathrm{dis}}\hat{a}\hat{U}^\dagger_{\mathrm{dis}} = \hat{a} - \xi_s, \tag{A6}$$

$$\hat{U}_{\mathrm{dis}}\hat{a}^\dagger\hat{U}^\dagger_{\mathrm{dis}} = \hat{a}^\dagger - \xi_s^*, \tag{A7}$$

$$\hat{U}_{\mathrm{rot}}\hat{a}\hat{U}^\dagger_{\mathrm{rot}} = \hat{a}e^{-i\omega_r t}, \tag{A8}$$

$$\hat{U}_{\mathrm{rot}}\hat{a}^\dagger\hat{U}^\dagger_{\mathrm{rot}} = \hat{a}^\dagger e^{i\omega_r t}. \tag{A9}$$

Now we can expand $\hat{H}_{\mathrm{KC}}$ to get

$$\begin{aligned}\hat{H}_{\mathrm{KC}} = {} & -\omega_r\hat{a}^\dagger\hat{a} + i\dot{\xi}_s\hat{a}^\dagger e^{i\omega_r t} - i\dot{\xi}_s^*\hat{a}e^{-i\omega_r t} \\ & + \omega_{a,0}(\hat{a}^\dagger e^{i\omega_r t} - \xi_s^*)(\hat{a}e^{-i\omega_r t} - \xi_s) \\ & + 2\mathrm{Re}(e^{i\omega_s t})[\epsilon_{s,0}(\hat{a}^\dagger e^{i\omega_r t} - \xi_s^*) + \epsilon^*_{s,0}(\hat{a}e^{-i\omega_r t} - \xi_s)] \\ & + g_3(\hat{a}e^{-i\omega_r t} - \xi_s + \mathrm{H.c.})^3 \\ & + g_4(\hat{a}e^{-i\omega_r t} - \xi_s + \mathrm{H.c.})^4. \end{aligned} \tag{A10}$$

Now, to determine ξ_s, we collect the terms with $\hat{a}^\dagger e^{i\omega_r t}$:

$$\begin{aligned} & -\xi_s\omega_{a,0} + i\dot{\xi}_s + 2\mathrm{Re}(e^{i\omega_s t})\epsilon_s = 0, \\ & \xi_s = -\left(\frac{\epsilon_{s,0}}{\omega_s - \omega_{a,0}}e^{-i\omega_s t} - \frac{\epsilon_{s,0}}{\omega_s + \omega_{a,0}}e^{i\omega_s t}\right). \end{aligned} \tag{A11}$$

Considering that both ξ_s and its complex conjugate will appear inside the nonlinear terms, we write $\xi_s + \xi_s^* = \xi_{s,\mathrm{eff}}e^{-i\omega_s t} + \mathrm{H.c.}$:

$$\xi_{s,\mathrm{eff}} = -\left(\frac{\epsilon_{s,0}}{\omega_s - \omega_{a,0}} - \frac{\epsilon_{s,0}}{\omega_s + \omega_{a,0}}\right). \tag{A12}$$

This means the first three lines in Eq. (A10) cancel up to some time-varying terms, which average to zero very quickly. Now, to eliminate the time dependence, we choose ω_r so that the term containing $\hat{a}^{\dagger 2}$ and $\hat{a}^2$ (which comes from the third-order nonlinearity) does not oscillate with time. This condition can be satisfied if $\omega_r = \omega_s/2$:

$$3g_3(\hat{a}^\dagger e^{i\omega_r t})^2\xi_{s,\mathrm{eff}} \cdot e^{-i\omega_s t} = 3g_3\hat{a}^{\dagger 2}\xi_{s,\mathrm{eff}} \cdot e^{-i(\omega_s - 2\omega_r)t}.$$

When this condition is satisfied, we can simplify $\hat{H}_{\mathrm{KC}}$ by neglecting every oscillating term to get

$$\hat{H}_{\mathrm{KC}} = \Delta_{a,\mathrm{r}}\hat{a}^\dagger\hat{a} - K\hat{a}^{\dagger 2}\hat{a}^2 + \epsilon_2\hat{a}^{\dagger 2} + \epsilon_2^*\hat{a}^2 - 4K\hat{a}^\dagger\hat{a}|\xi_{\mathrm{s,eff}}|^2. \tag{A13}$$

The first term is a harmonic term weighted by the detuning ($\Delta_{a,\mathrm{r}} = \omega_{a,0} - \omega_{\mathrm{r}}$). The second term is the Kerr nonlinearity ($K = -6g_4$). The third term is the two-photon drive ($\epsilon_2 = 3g_3\xi_{\mathrm{s,eff}}$), and the last term is the Stark shift induced by the drive. The coherent states $|\pm\alpha\rangle$ are eigenstates of this Hamiltonian with $\alpha^2 = \epsilon_2/K$ [28,29]. The cat states are the orthogonal even- and odd-parity states formed by the superposition of the coherent states and form two, degenerate ground states of this Hamiltonian:

$$|C_\alpha^\pm\rangle = \frac{1}{\sqrt{1 \pm e^{-2\alpha^2}}}\frac{1}{\sqrt{2}}(|\alpha\rangle \pm |-\alpha\rangle). \tag{A14}$$

2. Cat quadrature readout

The implementation of the cat quadrature readout is similar to the implementation of the two-photon drive, because it relies on the three-wave mixing in the SNAIL. To derive the Hamiltonian for cat quadrature readout, we first consider the combined Hamiltonian of the SNAIL and the readout resonator $\hat{H}_b$ with a coupling coefficient g_c much smaller than their detuning $\Delta = \omega_{a,0} - \omega_{b,0}$:

$$\hat{H}_0 = \hat{H}_a + \hat{H}_{\mathrm{s}} + \hat{H}_b + \hat{H}_{\mathrm{c}}, \tag{A15}$$

$$\hat{H}_b = \omega_{b,0}\hat{b}^\dagger\hat{b}, \tag{A16}$$

$$\hat{H}_c = g_{\mathrm{c}}(\hat{a}^\dagger + \hat{a})(\hat{b}^\dagger + \hat{b}) \approx g_{\mathrm{c}}(\hat{a}^\dagger\hat{b} + \hat{b}^\dagger\hat{a}). \tag{A17}$$

Now, we can cast this Hamiltonian in a dressed form where the bosonic modes are decoupled by using the following unitary [43]:

$$\hat{U}_{\mathrm{c}} = e^{\lambda(\hat{a}^\dagger\hat{b} - \hat{b}^\dagger\hat{a})}. \tag{A18}$$

The impact on the bosonic operators $\hat{a}$ and $\hat{b}$ is

$$\hat{U}_{\mathrm{c}}\hat{a}\hat{U}_{\mathrm{c}}^\dagger = \cos(\lambda)\hat{a} - \sin(\lambda)\hat{b} \approx \hat{a} - \frac{g_{\mathrm{c}}}{\Delta}\hat{b}, \tag{A19}$$

$$\hat{U}_{\mathrm{c}}\hat{b}\hat{U}_{\mathrm{c}}^\dagger = \cos(\lambda)\hat{b} + \sin(\lambda)\hat{a} \approx \hat{b} + \frac{g_{\mathrm{c}}}{\Delta}\hat{a}. \tag{A20}$$

Expanding $\hat{H}_a + \hat{H}_b + \hat{H}_{\mathrm{c}}$, we get

$$\begin{aligned}
&\omega_{a,0}(\cos(\lambda)\hat{a}^\dagger - \sin(\lambda)\hat{b}^\dagger)(\cos(\lambda)\hat{a} - \sin(\lambda)\hat{b}) \\
&+ \omega_{b,0}(\cos(\lambda)\hat{b}^\dagger + \sin(\lambda)\hat{a}^\dagger)(\cos(\lambda)\hat{b} + \sin(\lambda)\hat{a}) \\
&+ g_{\mathrm{c}}(\cos(\lambda)\hat{a}^\dagger - \sin(\lambda)\hat{b}^\dagger)(\cos(\lambda)\hat{b} + \sin(\lambda)\hat{a}) + \mathrm{H.c.} \\
&+ g_3(\cos(\lambda)\hat{a} - \sin(\lambda)\hat{b} + \mathrm{H.c.})^3 \\
&+ g_4(\cos(\lambda)\hat{a} - \sin(\lambda)\hat{b} + \mathrm{H.c.})^4.
\end{aligned} \tag{A21}$$

Choosing λ such that the coupling between the modes (i.e., the coefficient of $\hat{a}^\dagger\hat{b}$) vanishes gives

$$\lambda = \frac{1}{2}\mathrm{Arctan}\left(\frac{2g_{\mathrm{c}}}{\Delta}\right) \approx \frac{g_{\mathrm{c}}}{\Delta}. \tag{A22}$$

The renormalized frequencies are $\omega_a = \frac{1}{2}(\omega_{a,0} + \omega_{b,0} + \sqrt{\Delta^2 + 4g_{\mathrm{c}}^2}) \approx \omega_{a,0} + g_{\mathrm{c}}^2/\Delta$ and $\omega_b = \frac{1}{2}(\omega_{b,0} + \omega_{a,0} - \sqrt{\Delta^2 + 4g_{\mathrm{c}}^2}) \approx \omega_{b,0} - g_{\mathrm{c}}^2/\Delta$. Now, the two modes are decoupled, but the mode ω_b appears in the nonlinear terms of mode ω_a. So $\hat{H}_a + \hat{H}_b + \hat{H}_{\mathrm{c}}$ takes the effective form

$$\begin{aligned}
&\omega_a\hat{a}^\dagger\hat{a} + \omega_b\hat{b}^\dagger\hat{b} + g_3\left(\hat{a} + \frac{g_{\mathrm{c}}}{\Delta}\hat{b} + \mathrm{H.c.}\right)^3 \\
&+ g_4\left(\hat{a} + \frac{g_{\mathrm{c}}}{\Delta}\hat{b} + \mathrm{H.c.}\right)^4.
\end{aligned} \tag{A23}$$

The third term is the key to implementing the cat quadrature readout. Adding another drive of the form $\hat{H}_{\mathrm{CQR}} = 2\mathrm{Re}(e^{i\omega_{\mathrm{CQR}}t})(\epsilon_{\mathrm{CQR},0}\hat{a}^\dagger + \epsilon_{\mathrm{CQR},0}^*\hat{a})$ can implement the desired interaction, and following the same treatment as in Appendix A 1 we get

$$\begin{aligned}
&+ g_3\left(\hat{a}e^{-i\omega_{\mathrm{r}}t} + \frac{g_{\mathrm{c}}}{\Delta}\hat{b}e^{-i\omega_b t} - \xi_{\mathrm{CQR,eff}}e^{-i\omega_{\mathrm{CQR}}t}\right. \\
&\left. - \xi_{\mathrm{s,eff}}e^{-i\omega_{\mathrm{s}}t} + \mathrm{H.c.}\right)^3 \\
&+ g_4\left(\hat{a}e^{-i\omega_{\mathrm{r}}t} + \frac{g_{\mathrm{c}}}{\Delta}\hat{b}e^{-i\omega_b t} - \xi_{\mathrm{CQR,eff}}e^{-i\omega_{\mathrm{CQR}}t}\right. \\
&\left. - \xi_{\mathrm{s,eff}}e^{-i\omega_{\mathrm{s}}t} + \mathrm{H.c.}\right)^4.
\end{aligned} \tag{A24}$$

So, from g_3, we can also stabilize the following term in the rotating frame provided that $\omega_{\mathrm{CQR}} = \omega_b - \omega_{\mathrm{r}}$:

$$6g_3\frac{g_{\mathrm{c}}}{\Delta}\xi_{\mathrm{CQR,eff}}^*\hat{a}^\dagger\hat{b}e^{i(\omega_{\mathrm{CQR}} - \omega_b + \omega_{\mathrm{r}})t} + \mathrm{H.c.} \tag{A25}$$

From g_4, there will be two additional terms corresponding to the stark shift from the CQR drive and another term

corresponding to the cross Kerr between the readout and the SNAILmon:

$$24g_4\left(\hat{a}^\dagger\hat{a}+\frac{g_c^2}{\Delta^2}\hat{b}^\dagger\hat{b}\right)|\xi_{\mathrm{CQR,eff}}|^2+24g_4\frac{g_c^2}{\Delta^2}\hat{a}^\dagger\hat{a}\hat{b}^\dagger\hat{b}. \quad \text{(A26)}$$

APPENDIX B: MASTER EQUATION CALCULATIONS

In order to simulate the lifetime of the coherent states, we consider the system to be linearly coupled to a macroscopic environment composed of a bath of linear oscillators with continuous modes. The system environment coupling Hamiltonian in the rotating is

$$\hat{H}_{\mathrm{SB}}(t)=\sum_k V_k(\hat{a}e^{-i\omega_S t/2}+\hat{a}^\dagger e^{i\omega_S t/2})[\hat{b}_k(t)+\hat{b}_k^\dagger(t)], \quad \text{(B1)}$$

where V_k gives the coupling strength and $\hat{b}_k$ ($\hat{b}_k^\dagger$) are the annihilation (creation) operators of an excitation of energy $\hbar\omega_k$ in the environment. Following Ref. [68], we obtain following master equation up to $\mathcal{O}(\varphi_{\mathrm{zps}}^2)$:

$$\frac{d\hat{\rho}_S}{dt}=\frac{i}{\hbar}[\hat{H}_{\mathrm{KC}},\rho_S]+\hat{\mathcal{L}}_{\mathrm{RWA}}\hat{\rho}_S+\hat{\mathcal{L}}_{\mathrm{NRWA}}\hat{\rho}_S+\hat{\mathcal{L}}_\phi\hat{\rho}_S, \quad \text{(B2)}$$

where

$$\hat{\mathcal{L}}_{\mathrm{RWA}}=\kappa_{\omega_S/2}[n_{\omega_S/2}\mathcal{D}\{\hat{a}^\dagger\}+(1+n_{\omega_S/2})\mathcal{D}\{\hat{a}\}] \quad \text{(B3)}$$

gives the contributions satisfying the rotating wave approximation. It includes single-photon dissipation effects. $\kappa(\omega)$ is the spectral density of the environment defined through $\kappa(\omega)=2\pi\sum_k|V_k|^2\delta(\hbar\omega-\hbar\omega_k)$. The magnitude of spectral density depends strongly on the transition energy but is independent of any other system or environment parameters. The thermal population in the environment is given by the Bose-Einstein distribution function $n(\omega)=(e^{\hbar\omega/k_B\mathcal{T}_\omega}-1)^{-1}$, where $\mathcal{T}_\omega$ is the temperature of the environment. Similarly,

$$\hat{\mathcal{L}}_{\mathrm{NRWA}}=\kappa_{\omega_S}\left[n_{\omega_S}\mathcal{D}\left\{\frac{8g_3}{3\omega_S}\hat{a}^{\dagger 2}-\left(\frac{592g_3}{9\omega_S^2}-\frac{16g_4}{g_3\omega_S}\right)\hat{a}^\dagger\hat{a}\epsilon_2^*\right\}\right.$$
$$\left.+(1+n_{\omega_S})\mathcal{D}\left\{\frac{8g_3}{3\omega_S}\hat{a}^2-\left(\frac{592g_3}{9\omega_S^2}-\frac{16g_4}{g_3\omega_S}\right)\hat{a}^\dagger\hat{a}\epsilon_2\right\}\right] \quad \text{(B4)}$$

is the beyond-rotating wave approximation contributions. It includes two-photon dissipation effects and drive-induced dephasing, which enters the master equation at $\mathcal{O}(\varphi_{\mathrm{zps}}^2)$ with φ_{zps} being the value of the zero-point fluctuation in the phase operator of the SNAILmon [68]. Finally,

$$\hat{\mathcal{L}}_\phi=\kappa_\phi\mathcal{D}\{\hat{a}^\dagger\hat{a}\} \quad \text{(B5)}$$

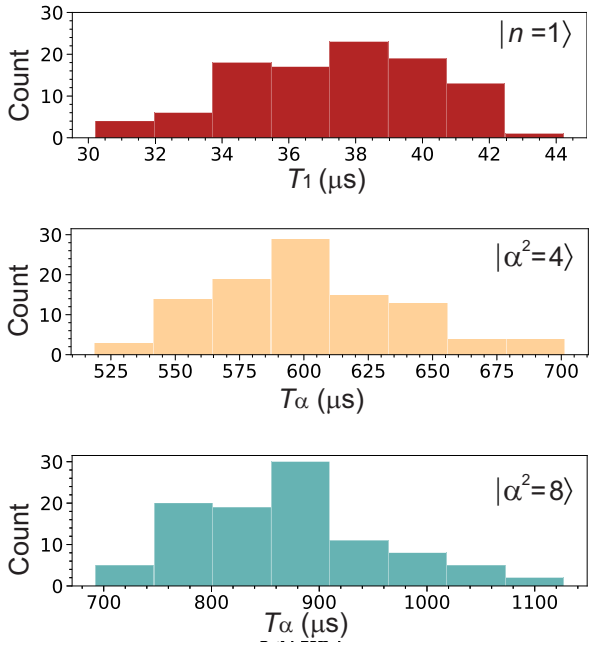

FIG. 5. Lifetime statistics. The lifetime for multiple states is examined over the span of two hours with 100 iterations. The lifetime of the first excited state in the Fock basis $|n=1\rangle$ can be used to estimate the single-photon loss at the qubit frequency. The long-lived coherent states $|\alpha^2=\epsilon_2/K\rangle$ also fluctuate over time, with an average lifetime of 601 μs for a cat of size 4 and 872 μs for a cat of size 8.

takes into account any additional drive-independent dephasing processes.

In our model, we consider single-photon effects, multiphoton heating and cooling effects, and dephasing as well as non-Markovian detuning noise. The non-Markovian noise is taken to be a Gaussian random fluctuation of the detuning with a mean of $0.03K$ and a standard deviation of $K/500$. The lifetime is averaged over 100 trials of the non-Markovian noise. We estimate $g_3/2\pi=15$ MHz and the decay rate $\kappa_{\omega_S/2}=1/T_1\approx 26$ kHz from the experiment. We fit the experimental data with $\mathcal{T}_{\omega_S/2}$, $\mathcal{T}_{\omega_S}$, κ_{ω_S}, and κ_ϕ. For the fit shown in Fig. 4(b), we use $\kappa_\phi=100$ Hz, $\kappa_{\omega_S}=7$ MHz, $\mathcal{T}_{\omega_S/2}=73.5$ mK, and $\mathcal{T}_{\omega_S}=515$ mK. We find an excellent agreement between the experimental data and theoretical plot up to the second plateau in the lifetime. The second plateau can be explained by changing the environment temperature (i.e., changing the value of n_{th} to be 5%) [35]. More statistics on the lifetime of the Fock qubit and the coherent states are shown in Fig. 5. Those variations in the lifetime are typical in superconducting qubits [70–73].

APPENDIX C: UNIVERSAL SINGLE-QUBIT GATES FOR THE KERR-CAT QUBIT

A universal gate set for the Kerr-cat qubit has been reported in the literature [20] based on continuous $Z(\theta)$

rotations and a discrete $X(\pi/2)$ rotation on the Bloch sphere. However, the discrete $X(\pi/2)$ relies on turning off the stabilization drive, which protects this qubit, and the performance of this gate degrades very quickly with increasing cat size $|\alpha|^2$ [35]. Therefore, it is necessary to realize an alternative approach with higher fidelity. Here, we describe the implementation of the gates we introduce in the main text.

1. Continuous $Z(\theta)$ rotation based on the quantum Zeno effect

Continuous $Z(\theta)$ rotations are realized by applying a microwave drive at the frequency $\omega_r = \omega_s/2$, which activates a single-photon transition between the cat states according to

$$\hat{H} = \frac{\Omega_z}{2}\hat{a}^\dagger + \frac{\Omega_z^*}{2}\hat{a}, \tag{C1}$$

where $\Omega_z/2$ is the strength of the microwave drive. The strong stabilization drive of the Kerr-cat qubit continuously projects its dynamics into the cat space due to the quantum Zeno effects. Therefore, if the single-photon transition rate is much smaller than the energy gap, i.e., $\Omega_z \ll E_{\text{gap}} = 4\epsilon_2$, one can project the bosonic mode operators into cat space to get

$$\hat{P}_C\hat{a}\hat{P}_C = \alpha\hat{Z} - i\alpha e^{-2\alpha^2}\hat{Y}, \tag{C2}$$

$$\hat{P}_C\hat{a}^\dagger\hat{P}_C = \alpha^*\hat{Z} + i\alpha^* e^{-2\alpha^2}\hat{Y}, \tag{C3}$$

where $\hat{P}_C = |C_\alpha^+\rangle\langle C_\alpha^+| + |C_\alpha^-\rangle\langle C_\alpha^-|$. We notice that both $\hat{a}$ and $\hat{a}^\dagger$ exponentially approach $\alpha\hat{Z}$ with increasing cat size. When Ω_z is in phase with α, the single-photon transition effectively applies continuous $Z(\theta)$ rotation according to the Hamiltonian:

$$\hat{P}_C\hat{H}\hat{P}_C^\dagger = 2\alpha\Omega_z\hat{Z}. \tag{C4}$$

2. $X(\pi/2)$ rotation based on pseudopotential deformation using phase modulation

Here, we describe the Hamiltonian that leads to the novel $X(\pi/2)$ gate introduced in Sec. IV in the main text. The $|+Z\rangle$ and $|-Z\rangle$ are approximately two coherent states localized in the two wells of the pseudopotential generated by the Kerr-cat Hamiltonian H_{KC} [Fig. 1(b)]. Therefore, an $X(\pi/2)$ gate requires interwell tunneling to achieve the desired population transfer. By introducing a positive detuning $\Delta\hat{a}^\dagger\hat{a}$ to the Kerr-cat Hamiltonian, the energy barrier between the two wells is lowered, allowing interwell tunneling:

$$\hat{H}_{\text{KC}}/\hbar = -K\hat{a}^{\dagger 2}\hat{a}^2 + \epsilon_2\hat{a}^{\dagger 2} + \epsilon_2^*\hat{a}^2 + \Delta\hat{a}^\dagger\hat{a}. \tag{C5}$$

Because $\Delta = \omega_Q - \omega_S/2$ is the detuning between the qubit frequency and half of the stabilization frequency, there are two ways to introduce such detuning. First, one can modulate the external flux by threading the SNAILs to change the qubit frequency ω_Q. However, this method also changes the Kerr nonlinearity and the SNAIL's third-order nonlinearity, making the analysis more complicated. Therefore, we use the second approach, which involves modulating the stabilization frequency ω_S directly. Practically, we modulate the phase of the stabilization drive according to

$$\epsilon_2(t) = \epsilon_2(0)e^{-it\dot{\delta}_d(t)}. \tag{C6}$$

This time dependence in the drive can be viewed as an effective time-dependent detuning under the following transformation:

$$\begin{aligned} H_{\text{rot}} &= \hat{U}_{\text{rot}}\hat{H}_{\text{KC}}\hat{U}_{\text{rot}}^\dagger + i\hbar\dot{\hat{U}}_{\text{rot}}\hat{U}_{\text{rot}}^\dagger \\ &= -K\hat{a}^{\dagger 2}\hat{a}^2 + \epsilon_2\hat{a}^{\dagger 2} + \epsilon_2^*\hat{a}^2 + \tilde{\Delta}(t)\hat{a}^\dagger\hat{a}, \end{aligned} \tag{C7}$$

$$\hat{U}_{\text{rot}} = e^{i\delta_d(t)t\hat{a}^\dagger a/2}. \tag{C8}$$

The unitary transformation is an effective rotating frame transformation with $\tilde{\Delta}(t) = -\frac{1}{2}[\delta_d(t) + t\dot{\delta}_d(t)]$ as the effective detuning. The pulse shape we use for the phase modulation is

$$\delta_d(t)/\delta_0 = \begin{cases} -\sin(\frac{3\pi}{2}t/T_g) & t \le T_g/3, \\ -\frac{f(t)}{1-f(T_g)}[f(t) - f(T_g)] & t > T_g/3. \end{cases} \tag{C9}$$

The function $f(t) = e^{-(t-T_g/3)^2/2\sigma^2}$ is a Gaussian with a standard deviation $\sigma = T_g/4$. This pulse shape prioritizes

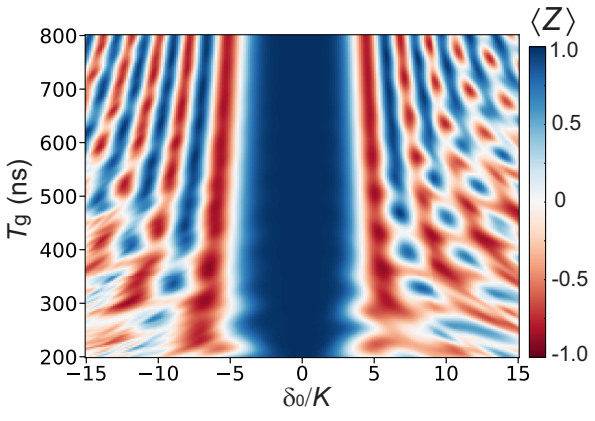

FIG. 6. Simulation of the detuning gate. Two $X(\pi/2)$ pulses are used to flip the value of $\langle Z\rangle$, similar to the experimental sequence in Fig. 3(b). Sweeping the gate time T_g and the maximum detuning δ_0 according to Eq. (C9) shows multiple regions where the potential deformation leads to coherent tunneling between the energy wells.

the first part of the pulse by making the ramp down much faster than the ramp up to compensate for the term proportional to the derivative. In practice, it offered around a factor of 2 faster gates compared to a $\sin^2(\pi t/T_g)$ pulse shape. The calibration process for the $X(\pi/2)$ gate is shown in Fig. 3(c); we implement two $X(\pi/2)$ pulses with variable gate time T_g and detuning modulation depth δ_0. The first readout is used to initialize the qubit along the z axis of the Bloch sphere. The measured expectation value of Pauli Z is shown in Fig. 3(d), reflecting a coherent state population transfer between the $|+Z\rangle$ and $|-Z\rangle$ states. The simulation of this gate is shown in Fig. 6. For short gate times (i.e., $T_g < 300$ ns), the process is not adiabatic with a Kerr of $K/2\pi = 1.2$ MHz.

APPENDIX D: KERR-CAT CALIBRATIONS

1. Cat size calibration

To calibrate the Kerr-cat qubit, we first rely on the Fock qubit calibration of the oscillator frequency ω_Q and the Kerr nonlinearity K. We use standard techniques like two-tone spectroscopy to measure ω_Q and estimate the Kerr nonlinearity first by measuring the two-photon transition $K = \omega_{02}/2 - \omega_Q$ in the frequency domain and then by using two-tone in pulse fashion in the 1–2 subspace [i.e., using pulse sequence $X_{01}(\pi)X_{12}(\pi,\omega)$] and the formula $K = -\alpha/2 = -(\omega_{12} - \omega_{01})/2$.

To calibrate the two-photon drive, we can start by driving the 0–2 transition by driving at $\omega_{20} = 2\omega_Q - 2K$, which leads to a Rabi rate of $\sqrt{8}\epsilon_2$. This method is accurate enough to get the right order of magnitude in the weak limit (i.e., $\epsilon_2 < 2K$). Next, to calibrate the amplitude of the two-photon accurately, we need to observe the change in the Rabi rate of the cat qubit according to $\approx 2\alpha|\Omega_z|\cos(\theta_z)\hat{Z} - 2\alpha\Omega_z\sin(\theta_z)e^{-2|\alpha|^2}\hat{Y}$, which is accurate in the limit $\epsilon_z \ll 4K\alpha^2$ and large enough cat size to see the exponential suppression (i.e., $\alpha^2 \gtrsim 2$). With the definition of the drive as $(\Omega_z/2)(\hat{a} + \hat{a}^\dagger)$, we measure Ω_z directly, since it is the Rabi rate of the Fock qubit. However, to measure the cat size, we need to calibrate the phase θ_z, which requires creating a chevron similar to Fig. 3(f). The full calibration of the cat size as a function of the strength of the two-photon drive is shown in Fig. 7(a), which calibrates the cat size α^2 according to

$$\alpha^2 = \left(\frac{\Omega_c}{2\Omega_z}\right)^2, \tag{D1}$$

where Ω_c is the Rabi rate of the cat qubit.

2. Mapping the Fock qubit to the cat qubit

With the large ratio of the Kerr nonlinearity relative to the device's single-photon decay rate, we can map the Fock qubit to the cat qubit and perform operations in each encoding. By parity conservation, the ground state of the Fock qubit ($|n=0\rangle$) maps to the even cat state, and the excited state ($|n=1\rangle$) maps to the odd cat state. However, to prepare the coherent states or the imaginary cat states, we can apply an $X_{01}(\pi/2)$ pulse in the Fock basis and then ramp up the stabilization drive, which prepares either the coherent states $|\pm\alpha\rangle$ or the imaginary cat states $|C^i_\pm\rangle$ according to the relative phase between the coherent state $\alpha = (\epsilon_2/K)^{1/2}$ and the initial $X(\pi/2)$ pulse as shown in

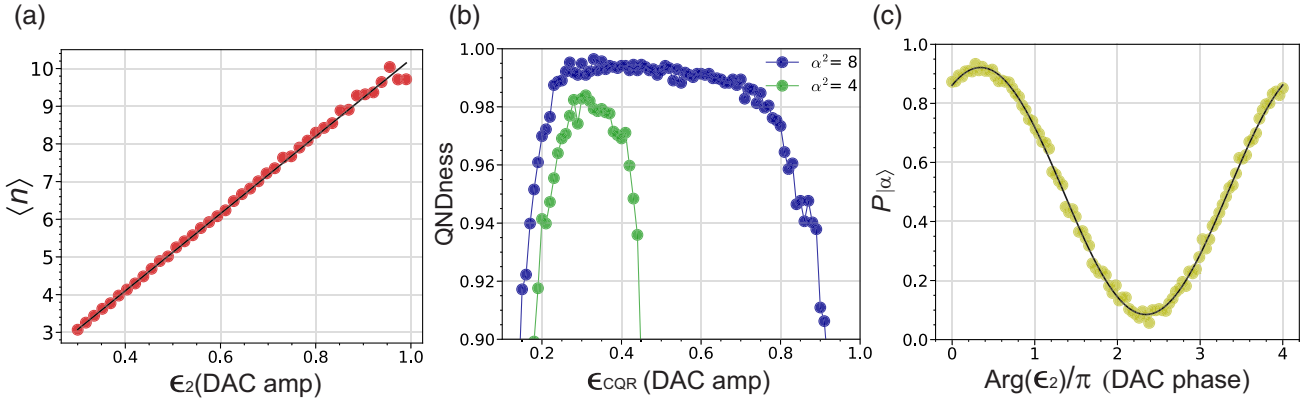

FIG. 7. Cat qubit calibrations. (a) The calibration of the cat size as a function of the two-photon drive strength (in units of DAC voltage) is done by measuring the increase in the Rabi rate of the cat qubit. The linear trend is expected from the formula $\langle n\rangle = \alpha^2 = \epsilon_2/K$, and it reflects the lack of any observable Stark shift from the drive. (b) The cat quadrature readout as a function of the DAC amplitude of the readout tone. We use a 4 μs readout signal for both cat sizes to maximize the SNR. The readout improves with increasing cat size, because we get the bosonic enhancement factor α, and for larger cats we can use larger readout signals, since the energy gap is proportional to the size (i.e., $4K\alpha^2$). (c) The mapping of the Fock qubit to the cat qubit enables us to use both encodings if necessary. The pulse sequence is an initial $X(\pi/2)$ pulse in the Fock basis followed by a 2 μs ramp of the stabilization drive and then cat readout. The electrical delay in the input lines determines the phase shift required to prepare the cat qubit in any desired point in the $z-y$ plane. With this protocol, we can prepare the coherent states $|\pm\alpha\rangle$ with a probability $P_\alpha = 93\%$. The data here are fitted to a sinusoidal function.

Fig. 7(c). This sequence enables us to use the cat quadrature readout to project the cat qubit along the z axis, which has better contrast than the dispersive readout in the Fock basis.

3. Optimizing the cat quadrature readout

The theoretical treatment of the cat quadrature readout was introduced in Appendix A 2, and more details can be found in Refs. [20,35]. It involves a microwave-activated beam-splitter interaction between the cat qubit mode $\hat{a}$ and the readout resonator $\hat{b}$. When interaction strength $\epsilon_{\mathrm{CQR}} = 6g_3(g_c/\Delta)\xi_{\mathrm{CQR,eff}}$ is much smaller than the energy gap $4K\alpha^2$, Eq. (A25) can be projected into the computational space, giving the effective form

$$\hat{H}_{\mathrm{CQR}} = \alpha\epsilon_{\mathrm{CQR}}\hat{Z}(\hat{b} + \hat{b}^{\dagger}), \tag{D2}$$

which is commonly referred to as longitudinal readout in the field of superconducting qubits [12]. In this readout scheme, a photon from the drive combines with a photon from the qubit through the third-order nonlinearity of the SNAIL to create a photon in the readout mode. The stabilization drive replenishes the qubit much faster than any change in its state, keeping this process quantum nondemolition to first order.

To quantify the QNDness, we need two consecutive readouts, as shown in Fig. 3(a), and the results for cat sizes $\alpha^2 = 4, 8$ are shown in Fig. 7(b) as a function of the readout strength. We perform each measurement in 4 μs, which is more than 2 orders of magnitude smaller than the lifetime of the coherent states for both cat sizes. The main factor for improvement in this work compared to Ref. [20] is the longer lifetime of the coherent states and the large energy gap $E_{\mathrm{gap}} = 4K\alpha^2$ compared to Ref. [35] enabling larger readout power.

APPENDIX E: GATE CHARACTERIZATION WITH PROCESS TOMOGRAPHY

To get an estimate of the quality of the single-qubit gates, we use process tomography in the cat encoding and leverage the cat quadrature readout, which we expect to

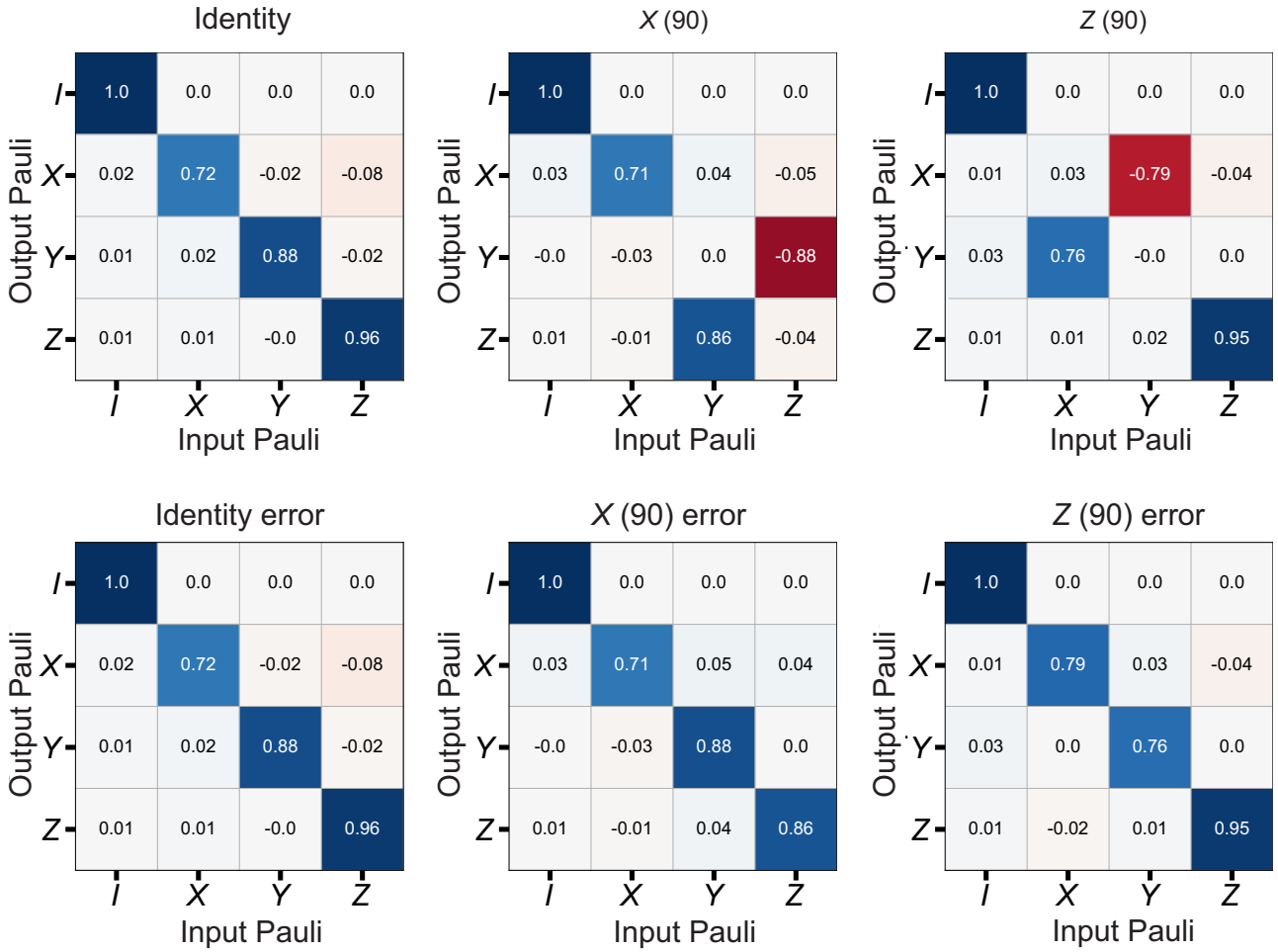

FIG. 8. Gate characterization. Pauli transfer matrix for the identity $X(\pi/2)$ and $Z(\pi/2)$. State preparation and measurement in the X basis is the limiting factor in all three cases. Faster $Z(\pi/2)$ gates can improve this number at the expense of a shorter lifetime for the coherent states.

contribute minimally to state preparation and measurement errors. For a cat of size $\alpha^2 = 4$, the lifetime along the z axis is around $T_\alpha \approx 600$ μs, and the lifetime along the X and Y axes is around $T_C \approx 5$ μs. We perform the $Z(\pi/2)$ gate in 120 ns and the $X(\pi/2)$ gate in 320 ns. To calculate the gate fidelity, we use $\mathcal{F}_g = \frac{1}{3}[\frac{1}{2}\mathrm{Tr}(\mathcal{R}^T_{\mathrm{ideal}}\mathcal{R}_{\mathrm{exp}}) + 1]$, with $\mathcal{R}^T_{\mathrm{ideal}}$ being the ideal Pauli transfer matrix (PTM) and $\mathcal{R}_{\mathrm{exp}}$ being the experimental value.

To calculate the experimental PTM, we start by using the cat quadrature readout to initialize the qubit in the state $|\alpha\rangle$, and then we prepare four different states by applying I, $Y(90)$, $X(270)$, and $X(180)$. The final gate is a virtual gate that flips the sign of any subsequent Ω_z drive or ϵ_{CQR} readout tone. After that, we apply the desired operation and construct the output density matrix for every input state. Finally, we perform least-square approximation to find the single-qubit PTM. The process matrix for the identity, the $X(\pi/2)$ gate, and the $Z(\pi/2)$ gate from this analysis are shown in Fig. 8. However, this method neglects leakage by enforcing normalization, which can be estimated in future devices with larger Kerr by mapping back to the Fock basis to measure the population of the $|n = 3\rangle$ state. Also, in this method, the error is limited by state preparation, since $\mathcal{F}_{X_{\pi/2}} = 90.8\%$ and $\mathcal{F}_{Z_{\pi/2}} = 91.7\%$, and, for the identity, we measure $\mathcal{F}_I = 92.7\%$. The characterization of those gates in a SPAM-free way that distinguishes the noise bias of every gate in the set is the subject of the next study on this device.

APPENDIX F: EXPERIMENTAL PARAMETERS

The experimental parameters of this device are chosen to maximize the lifetime of the qubit and achieve high QND readout while maintaining fast control in the cat subspace. The data are summarized in Table I. The qubit frequency ω_{Q} is chosen to be compatible with cryogenic components and room-temperature microwave electronics

TABLE I. Experimental parameters.

Parameter	Value
SNAILmon qubit frequency $\omega_Q/2\pi$	5.9 GHz
SNAILmon capacitive shunt energy E_c/h	118 MHz
Number of SNAILs	2
SNAILmon junction asymmetry	0.1
SNAILmon Kerr nonlinearity $K/2\pi$	1.2 MHz
Fock qubit single-photon decay time T_1	38.5 μs
Fock qubit Ramsey decay time T_2^*	3 μs
Readout resonator frequency $\omega_R/2\pi$	7.1 GHz
Readout resonator linewidth $\kappa_R/2\pi$	0.4 MHz
Readout to SNAILmon coupling strength $g/2\pi$	125 MHz
Readout to SNAILmon cross-Kerr $\chi/2\pi$	40 kHz
Readout resonator internal quality factor $Q_{R,i}$	3×10^5
Purcell filter frequency $\omega_P/2\pi$	7.2 GHz
Purcell filter linewidth $\kappa_P/2\pi$	60 MHz

while maintaining a large ratio of E_J/E_c to maximize the number of bound states in the oscillator (E_J is the effective Josephson energy of the SNAIL). The capacitive shunt energy E_{c}/h was chosen to be a value between 300 MHz, which is commonly used to make transmon qubits with high coherence and the smaller values previously reported in 3D cat experiments ($E_{\mathrm{c}} \approx 64$ MHz), which increases the ratio of the nonlinearities g_3/g_4 of the SNAIL. Using two SNAILs instead of one increases the number of bound states by a factor of 4 and increases the ratio of g_3/g_4 by a factor of 2 [47]. The 1.2 MHz Kerr is an optimal value in practice to maximize the lifetime of the coherent states while maintaining fast single-qubit gates. The readout mode linewidth is chosen to be 0.1–1 MHz to maximize the SNR of the cat quadrature readout [20]. The dedicated, sharp Purcell filter for readout is crucial to maintaining a high limit on the qubit lifetime while keeping the coupling strength between the qubit and readout large (i.e., $g/\Delta \approx 0.1$). The original Purcell limit on the lifetime of the SNAILmon (i.e., T_1) from the strongly coupled port is estimated to be approximately 12 μs from finite-element simulation using Ansys high-frequency electromagnetic field simulation (HFSS). The 30 dB of isolation at the qubit frequency increases this limit to 12 ms.

APPENDIX G: BAND-BLOCK FILTER

The band-block filter enables strong coupling to the qubit, eliminating the need for very large input power. In the early stages of this experiment, the mixing chamber of the dilution fridge used to heat up by a few mK when we used the control line for pumping. The chip we used to characterize the filter is shown in Fig. 9(a) with an enlarged view into one of the stubs in Fig. 9(b). The open boundary condition requires this filter design to be $\lambda/4$ to have destructive interference inside the stop band of the filter [51]. Figure 9(c) shows a visualization of this process. The normalized transmission coefficient $\overline{S}_{21}$ of the filter shown in Fig. 2 includes 69 dB of attenuation in the lines and 10 dB insertion loss just outside the filter range. Adapting this filter design in other experiments involving strong off-resonance drives should make those processes efficient with minimal heating effects.

APPENDIX H: MICROWAVE CONTROL HARDWARE

As a strongly driven qubit, the Kerr-cat qubit requires multiple, strong drives at different frequency ranges with high spectral purity and fast control. To accomplish this, we use the standard techniques of up-conversion and down-conversion of rf signals that we generate with the arbitrary waveform generator (AWG) and analyze with an analog-to-digital converter (ADC) at 1 GS/s sampling rate.

The wiring diagram shown in Fig. 10 includes the different stages of the dilution fridge. The AWG enables

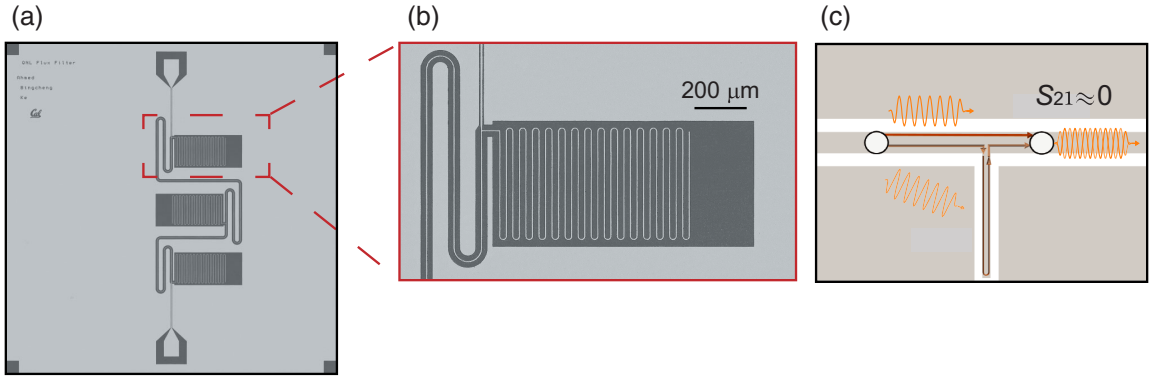

FIG. 9. Band-block filter. (a) The 5×5 mm^2 test device used to measure the scattering parameters in Fig. 2. (b) An enlarged view into one stub of the filter where the length is chosen to have destructive interference around the qubit frequency. (c) The destructive interference results from the π phase the signal picks from the two paths.

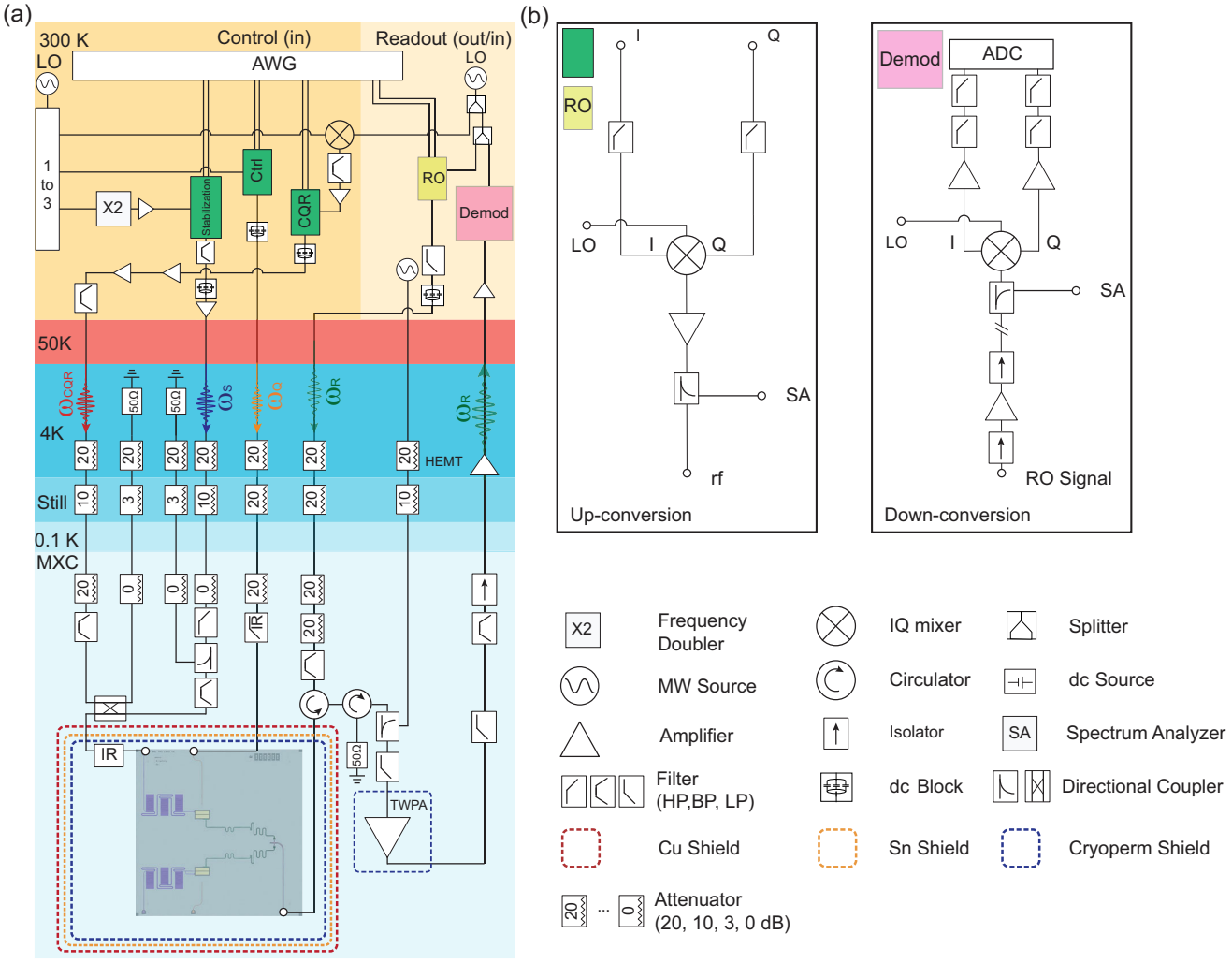

FIG. 10. Wiring diagram. (a) The microwave components used in this experiment for control and readout involve an arbitrary waveform generator (AWG), local oscillators (LOs), and an analog-to-digital converter (ADC). The rest of the microwave components are shown. (b) The two schemes of up-conversion and down-conversion of the signals using the AWG and ADC equipment at a 1 GS/s sampling rate.

using the lower sidebands of the IQ mixer with IF frequencies of 70 MHz for the qubit control signals, 140 MHz for the stabilization drive, and 140 MHz for the cat quadrature readout up-conversion. For the down-conversion of the readout signal, we use 210 MHz IF frequency. The difference between the up-conversion and down-conversion IF frequencies is the result of the input signal being at ω_{CQR} and the output signal being at ω_{R}. In this experiment, we use two local oscillators around the qubit frequency and the readout frequency. To generate the carrier of the stabilization drive, we use a frequency doubler, and, to generate the carrier of the cat quadrature readout, we mix the two local oscillators with an rf mixer (shown in the diagram). This arrangement eliminates the sensitivity on the phase of the local oscillators when controlling the qubit [i.e., driving on phase as in Fig. 3(f)] or performing the cat readout [i.e., the IQ signal shown in Fig. 3(b)]. Also, since the Kerr-cat Hamiltonian is realized in the rotating frame, the readout signal picks a phase depending on the delay we use relative to the time we ramp up the stabilization drive. To account for this delay, we multiply the input signal ϵ_{CQR} with the appropriate phase to make sure the output signal always aligns with the reference we use to draw the discrimination line in the IQ plane. In this experiment, we ensure spectral purity of approximately 40 dB suppression of the next visible side band, which requires large IF frequencies and the use of both high-pass and low-pass filters to suppress the sidebands and dc bias at each mixer to suppress the carrier.

To ensure the thermalization of the qubit, we attenuate the lines heavily and use a gold-plated cryogenic attenuator from Quantum Microwave at the mixing chamber in combination with Eccosorb filters. To avoid dumping heat at the mixing chamber (MXC), we use directional couplers to attenuate the signal at the MXC plate while directing the signal to the 4 K with 50-Ohm termination. The output signal is first amplified with a traveling wave parametric amplifier (TWPA) with a gain of around 20 dB at the mixing chamber [74], then a HEMT amplifier at 4 K, and a low-noise amplifier at room temperature. The signal is then down-converted with an IQ mixer, filtered around the demodulation frequency, and amplified before sending it to the ADC.

[1] J. A. Schreier, A. A. Houck, J. Koch, D. I. Schuster, B. R. Johnson, J. M. Chow, J. M. Gambetta, J. Majer, L. Frunzio, M. H. Devoret, S. M. Girvin, and R. J. Schoelkopf, *Suppressing charge noise decoherence in superconducting charge qubits*, Phys. Rev. B **77**, 180502(R) (2008).

[2] J. Koch, T. M. Yu, J. Gambetta, A. A. Houck, D. I. Schuster, J. Majer, A. Blais, M. H. Devoret, S. M. Girvin, and R. J. Schoelkopf, *Charge-insensitive qubit design derived from the Cooper pair box*, Phys. Rev. A **76**, 042319 (2007).

[3] V. E. Manucharyan, J. Koch, L. I. Glazman, and M. H. Devoret, *Fluxonium: Single Cooper-pair circuit free of charge offsets*, Science **326**, 113 (2009).

[4] L. B. Nguyen, Y.-H. Lin, A. Somoroff, R. Mencia, N. Grabon, and V. E. Manucharyan, *High-coherence fluxonium qubit*, Phys. Rev. X **9**, 041041 (2019).

[5] A. Gyenis, P. S. Mundada, A. Di Paolo, T. M. Hazard, X. You, D. I. Schuster, J. Koch, A. Blais, and A. A. Houck, *Experimental realization of a protected superconducting circuit derived from the 0–π qubit*, PRX Quantum **2**, 010339 (2021).

[6] P. Brooks, A. Kitaev, and J. Preskill, *Protected gates for superconducting qubits*, Phys. Rev. A **87**, 052306 (2013).

[7] D. Gottesman, A. Kitaev, and J. Preskill, *Encoding a qubit in an oscillator*, Phys. Rev. A **64**, 012310 (2001).

[8] P. Campagne-Ibarcq, A. Eickbusch, S. Touzard, E. Zalys-Geller, N. E. Frattini, V. V. Sivak, P. Reinhold, S. Puri, S. Shankar, R. J. Schoelkopf *et al.*, *Quantum error correction of a qubit encoded in grid states of an oscillator*, Nature (London) **584**, 368 (2020).

[9] I. Siddiqi, *Engineering high-coherence superconducting qubits*, Nat. Rev. Mater. **6**, 875 (2021).

[10] M. Kjaergaard, M. E. Schwartz, J. Braumüller, P. Krantz, J. I.-J. Wang, S. Gustavsson, and W. D. Oliver, *Superconducting qubits: Current state of play*, Annu. Rev. Condens. Matter Phys. **11**, 369 (2020).

[11] A. Blais, A. L. Grimsmo, S. M. Girvin, and A. Wallraff, *Circuit quantum electrodynamics*, Rev. Mod. Phys. **93**, 025005 (2021).

[12] P. Krantz, M. Kjaergaard, F. Yan, T. P. Orlando, S. Gustavsson, and W. D. Oliver, *A quantum engineer's guide to superconducting qubits*, Appl. Phys. Rev. **6**, 021318 (2019).

[13] B. Vlastakis, G. Kirchmair, Z. Leghtas, S. E. Nigg, L. Frunzio, S. M. Girvin, M. Mirrahimi, M. H. Devoret, and R. J. Schoelkopf, *Deterministically encoding quantum information using 100-photon Schrödinger cat states*, Science **342**, 607 (2013).

[14] Y. Y. Gao, B. J. Lester, K. S. Chou, L. Frunzio, M. H. Devoret, L. Jiang, S. Girvin, and R. J. Schoelkopf, *Entanglement of bosonic modes through an engineered exchange interaction*, Nature (London) **566**, 509 (2019).

[15] N. Ofek, A. Petrenko, R. Heeres, P. Reinhold, Z. Leghtas, B. Vlastakis, Y. Liu, L. Frunzio, S. M. Girvin, L. Jiang *et al.*, *Extending the lifetime of a quantum bit with error correction in superconducting circuits*, Nature (London) **536**, 441 (2016).

[16] C. Wang, Y. Y. Gao, P. Reinhold, R. W. Heeres, N. Ofek, K. Chou, C. Axline, M. Reagor, J. Blumoff, K. Sliwa *et al.*, *A Schrödinger cat living in two boxes*, Science **352**, 1087 (2016).

[17] C. Song, K. Xu, H. Li, Y.-R. Zhang, X. Zhang, W. Liu, Q. Guo, Z. Wang, W. Ren, J. Hao *et al.*, *Generation of multicomponent atomic Schrödinger cat states of up to 20 qubits*, Science **365**, 574 (2019).

[18] X. Pan, J. Schwinger, N.-N. Huang, P. Song, W. Chua, F. Hanamura, A. Joshi, F. Valadares, R. Filip, and Y. Y. Gao, *Protecting the quantum interference of cat states by phase-space compression*, Phys. Rev. X **13**, 021004 (2023).

[19] Z. Leghtas, S. Touzard, I. M. Pop, A. Kou, B. Vlastakis, A. Petrenko, K. M. Sliwa, A. Narla, S. Shankar, M. J. Hatridge, M. Reagor, L. Frunzio, R. J. Schoelkopf, M. Mirrahimi, and M. H. Devoret, *Confining the state of light to a quantum manifold by engineered two-photon loss*, Science **347**, 853 (2015).

[20] A. Grimm, N. E. Frattini, S. Puri, S. O. Mundhada, S. Touzard, M. Mirrahimi, S. M. Girvin, S. Shankar, and M. H. Devoret, *Stabilization and operation of a Kerr-cat qubit*, Nature (London) **584**, 205 (2020).

[21] Q. Xu, G. Zheng, Y.-X. Wang, P. Zoller, A. A. Clerk, and L. Jiang, *Autonomous quantum error correction and fault-tolerant quantum computation with squeezed cat qubits*, npj Quantum Inf. **9**, 78 (2023).

[22] L. B. Nguyen, N. Goss, K. Siva, Y. Kim, E. Younis, B. Qing, A. Hashim, D. I. Santiago, and I. Siddiqi, *Empowering high-dimensional quantum computing by traversing the dual bosonic ladder*, Nat. Commun. **15**, 7117 (2024).

[23] C. Monroe, D. M. Meekhof, B. E. King, and D. J. Wineland, *A Schrödinger cat superposition state of an atom*, Science **272**, 1131 (1996).

[24] A. Omran, H. Levine, A. Keesling, G. Semeghini, T. T. Wang, S. Ebadi, H. Bernien, A. S. Zibrov, H. Pichler, S. Choi *et al.*, *Generation and manipulation of Schrödinger cat states in Rydberg atom arrays*, Science **365**, 570 (2019).

[25] R. Lescanne, M. Villiers, T. Peronnin, A. Sarlette, M. Delbecq, B. Huard, T. Kontos, M. Mirrahimi, and Z. Leghtas, *Exponential suppression of bit-flips in a qubit encoded in an oscillator*, Nat. Phys. **16**, 509 (2020).

[26] C. Berdou, A. Murani, U. Réglade, W. C. Smith, M. Villiers, J. Palomo, M. Rosticher, A. Denis, P. Morfin, M. Delbecq, T. Kontos, N. Pankratova, F. Rautschke, T. Peronnin, L.-A. Sellem, P. Rouchon, A. Sarlette, M. Mirrahimi, P. Campagne-Ibarcq, S. Jezouin, R. Lescanne, and Z. Leghtas, *One hundred second bit-flip time in a two-photon dissipative oscillator*, PRX Quantum **4**, 020350 (2023).

[27] U. Réglade, A. Bocquet, R. Gautier, A. Marquet, E. Albertinale, N. Pankratova, M. Hallén, F. Rautschke, L.-A. Sellem, P. Rouchon *et al.*, *Quantum control of a cat-qubit with bit-flip times exceeding ten seconds*, Nature (London) **629**, 778 (2024).

[28] S. Puri, S. Boutin, and A. Blais, *Engineering the quantum states of light in a Kerr-nonlinear resonator by two-photon driving*, npj Quantum Inf. **3**, 18 (2017).

[29] H. Goto, *Universal quantum computation with a nonlinear oscillator network*, Phys. Rev. A **93**, 050301(R) (2016).

[30] S. Puri, L. St-Jean, J. A. Gross, A. Grimm, N. E. Frattini, P. S. Iyer, A. Krishna, S. Touzard, L. Jiang, A. Blais, S. T. Flammia, and S. M. Girvin, *Bias-preserving gates with stabilized cat qubits*, Sci. Adv. **6**, eaay5901 (2020).

[31] S. Puri, A. Grimm, P. Campagne-Ibarcq, A. Eickbusch, K. Noh, G. Roberts, L. Jiang, M. Mirrahimi, M. H. Devoret, and S. M. Girvin, *Stabilized cat in a driven nonlinear cavity: A fault-tolerant error syndrome detector*, Phys. Rev. X **9**, 041009 (2019).

[32] D. Ruiz, R. Gautier, J. Guillaud, and M. Mirrahimi, *Two-photon driven Kerr quantum oscillator with multiple spectral degeneracies*, Phys. Rev. A **107**, 042407 (2023).

[33] L. Gravina, F. Minganti, and V. Savona, *Critical Schrödinger cat qubit*, PRX Quantum **4**, 020337 (2023).

[34] R. Gautier, A. Sarlette, and M. Mirrahimi, *Combined dissipative and Hamiltonian confinement of cat qubits*, PRX Quantum **3**, 020339 (2022).

[35] N. E. Frattini, R. G. Cortiñas, J. Venkatraman, X. Xiao, Q. Su, C. U. Lei, B. J. Chapman, V. R. Joshi, S. Girvin, R. J. Schoelkopf *et al.*, *The squeezed Kerr oscillator: Spectral kissing and phase-flip robustness*, Phys. Rev. X **14**, 031040 (2024).

[36] X. L. He, Y. Lu, D. Q. Bao, H. Xue, W. B. Jiang, Z. Wang, A. F. Roudsari, P. Delsing, J. S. Tsai, and Z. R. Lin, *Fast generation of Schrödinger cat states using a Kerr-tunable superconducting resonator*, Nat. Commun. **14**, 6358 (2023).

[37] D. Iyama, T. Kamiya, S. Fujii, H. Mukai, Y. Zhou, T. Nagase, A. Tomonaga, R. Wang, J.-J. Xue, S. Watabe *et al.*, *Observation and manipulation of quantum interference in a superconducting Kerr parametric oscillator*, Nat. Commun. **15**, 86 (2024).

[38] J. Venkatraman, R. G. Cortinas, N. E. Frattini, X. Xiao, and M. H. Devoret, *A driven quantum superconducting circuit with multiple tunable degeneracies*, arXiv:2211.04605.

[39] A. S. Darmawan, B. J. Brown, A. L. Grimsmo, D. K. Tuckett, and S. Puri, *Practical quantum error correction with the XZZX code and Kerr-cat qubits*, PRX Quantum **2**, 030345 (2021).

[40] Q. Xu, N. Mannucci, A. Seif, A. Kubica, S. T. Flammia, and L. Jiang, *Tailored XZZX codes for biased noise*, Phys. Rev. Res. **5**, 013035 (2023).

[41] J. P. Bonilla Ataides, D. K. Tuckett, S. D. Bartlett, S. T. Flammia, and B. J. Brown, *The XZZX surface code*, Nat. Commun. **12**, 2172 (2021).

[42] H. Paik, D. I. Schuster, L. S. Bishop, G. Kirchmair, G. Catelani, A. P. Sears, B. R. Johnson, M. J. Reagor, L. Frunzio, L. I. Glazman, S. M. Girvin, M. H. Devoret, and R. J. Schoelkopf, *Observation of high coherence in Josephson junction qubits measured in a three-dimensional circuit QED architecture*, Phys. Rev. Lett. **107**, 240501 (2011).

[43] A. Blais, R.-S. Huang, A. Wallraff, S. M. Girvin, and R. J. Schoelkopf, *Cavity quantum electrodynamics for superconducting electrical circuits: An architecture for quantum computation*, Phys. Rev. A **69**, 062320 (2004).

[44] A. Wallraff, D. I. Schuster, A. Blais, L. Frunzio, R.-S. Huang, J. Majer, S. Kumar, S. M. Girvin, and R. J. Schoelkopf, *Strong coupling of a single photon to a superconducting qubit using circuit quantum electrodynamics*, Nature (London) **431**, 162 (2004).

[45] L. B. Nguyen, Y. Kim, A. Hashim, N. Goss, B. Marinelli, B. Bhandari, D. Das, R. K. Naik, J. M. Kreikebaum, A. N. Jordan *et al.*, *Programmable Heisenberg interactions between Floquet qubits*, Nat. Phys. **20**, 240 (2024).

[46] N. E. Frattini, U. Vool, S. Shankar, A. Narla, K. M. Sliwa, and M. H. Devoret, *3-wave mixing Josephson dipole element*, Appl. Phys. Lett. **110**, 222603 (2017).

[47] N. E. Frattini, V. V. Sivak, A. Lingenfelter, S. Shankar, and M. H. Devoret, *Optimizing the nonlinearity and dissipation of a SNAIL parametric amplifier for dynamic range*, Phys. Rev. Appl. **10**, 054020 (2018).

[48] I. García-Mata, R. G. Cortiñas, X. Xiao, J. Chávez-Carlos, V. S. Batista, L. F. Santos, and D. A. Wisniacki, *Effective versus Floquet theory for the Kerr parametric oscillator*, Quantum **8**, 1298 (2024).

[49] M. S. Blok, V. V. Ramasesh, T. Schuster, K. O'Brien, J. M. Kreikebaum, D. Dahlen, A. Morvan, B. Yoshida, N. Y. Yao, and I. Siddiqi, *Quantum information scrambling on a superconducting qutrit processor*, Phys. Rev. X **11**, 021010 (2021).

[50] J. Kreikebaum, K. O'Brien, A. Morvan, and I. Siddiqi, *Improving wafer-scale Josephson junction resistance variation in superconducting quantum coherent circuits*, Supercond. Sci. Technol. **33**, 06LT02 (2020).

[51] D. M. Pozar, *Microwave Engineering* (Wiley, New York, 2011).

[52] M. V. P. Altoé, A. Banerjee, C. Berk, A. Hajr, A. Schwartzberg, C. Song, M. Alghadeer, S. Aloni, M. J. Elowson, J. M. Kreikebaum, E. K. Wong, S. M. Griffin, S. Rao, A. Weber-Bargioni, A. M. Minor, D. I. Santiago, S. Cabrini, I. Siddiqi, and D. F. Ogletree, *Localization and mitigation of loss in niobium superconducting circuits*, PRX Quantum **3**, 020312 (2022).

[53] J. Verjauw, R. Acharya, J. Van Damme, T. Ivanov, D. P. Lozano, F. Mohiyaddin, D. Wan, J. Jussot, A. Vadiraj, M. Mongillo *et al.*, *Path toward manufacturable superconducting qubits with relaxation times exceeding 0.1 ms*, npj Quantum Inf. **8**, 93 (2022).

[54] C. Wang, X. Li, H. Xu, Z. Li, J. Wang, Z. Yang, and H. Yu, *Towards practical quantum computers: Transmon qubit with a lifetime approaching 0.5 milliseconds*, npj Quantum Inf. **8**, 1 (2022).

[55] K. D. Crowley, R. A. McLellan, A. Dutta, N. Shumiya, A. P. M. Place, X. H. Le, Y. Gang, T. Madhavan, M. P. Bland, R. Chang, N. Khedkar, Y. C. Feng, E. A. Umbarkar, X. Gui, L. V. H. Rodgers, Y. Jia, M. M. Feldman, S. A. Lyon, M. Liu, R. J. Cava, A. A. Houck, and N. P. de Leon, *Disentangling losses in tantalum superconducting circuits*, Phys. Rev. X **13**, 041005 (2023).

[56] A. P. Place, L. V. Rodgers, P. Mundada, B. M. Smitham, M. Fitzpatrick, Z. Leng, A. Premkumar, J. Bryon, A. Vrajitoarea, S. Sussman *et al.*, *New material platform for superconducting transmon qubits with coherence times exceeding 0.3 milliseconds*, Nat. Commun. **12**, 1779 (2021).

[57] A. Romanenko and D. I. Schuster, *Understanding quality factor degradation in superconducting niobium cavities at low microwave field amplitudes*, Phys. Rev. Lett. **119**, 264801 (2017).

[58] C. Leroux, A. Di Paolo, and A. Blais, *Superconducting coupler with exponentially large on:off ratio*, Phys. Rev. Appl. **16**, 064062 (2021).

[59] B. J. Chapman, S. J. de Graaf, S. H. Xue, Y. Zhang, J. Teoh, J. C. Curtis, T. Tsunoda, A. Eickbusch, A. P. Read, A. Koottandavida, S. O. Mundhada, L. Frunzio, M. H. Devoret, S. M. Girvin, and R. J. Schoelkopf, *High-on-off-ratio beamsplitter interaction for gates on bosonically encoded qubits*, PRX Quantum **4**, 020355 (2023).

[60] C. Zhou, P. Lu, M. Praquin, T.-C. Chien, R. Kaufman, X. Cao, M. Xia, R. S. Mong, W. Pfaff, D. Pekker *et al.*, *Realizing all-to-all couplings among detachable quantum modules using a microwave quantum state router*, npj Quantum Inf. **9**, 54 (2023).

[61] M. D. Reed, B. R. Johnson, A. A. Houck, L. DiCarlo, J. M. Chow, D. I. Schuster, L. Frunzio, and R. J. Schoelkopf, *Fast reset and suppressing spontaneous emission of a superconducting qubit*, Appl. Phys. Lett. **96**, 203110 (2010).

[62] N. T. Bronn, E. Magesan, N. A. Masluk, J. M. Chow, J. M. Gambetta, and M. Steffen, *Reducing spontaneous emission in circuit quantum electrodynamics by a combined readout/filter technique*, IEEE Trans. Appl. Supercond. **25**, 1 (2015).

[63] A. Sah, S. Kundu, H. Suominen, Q. Chen, and M. Möttönen, *Decay-protected superconducting qubit with fast control enabled by integrated on-chip filters*, Commun. Phys. **7**, 227 (2024).

[64] Y. Zhou, X. Cai, Y. Zheng, B. Zhou, Y. Wang, K. Xiong, and J. Feng, *High-suppression-ratio and wide bandwidth four-stage Purcell filter for multiplexed superconducting qubit readout*, J. Appl. Phys. **135**, 024402 (2024).

[65] Y. Sunada, S. Kono, J. Ilves, S. Tamate, T. Sugiyama, Y. Tabuchi, and Y. Nakamura, *Fast readout and reset of a superconducting qubit coupled to a resonator with an intrinsic Purcell filter*, Phys. Rev. Appl. **17**, 044016 (2022).

[66] F. Swiadek, R. Shillito, P. Magnard, A. Remm, C. Hellings, N. Lacroix, Q. Ficheux, D. C. Zanuz, G. J. Norris, A. Blais *et al.*, *Enhancing dispersive readout of superconducting qubits through dynamic control of the dispersive shift: Experiment and theory*, arXiv:2307.07765.

[67] Y.-H. Kang, Y.-H. Chen, X. Wang, J. Song, Y. Xia, A. Miranowicz, S.-B. Zheng, and F. Nori, *Nonadiabatic geometric quantum computation with cat-state qubits via invariant-based reverse engineering*, Phys. Rev. Res. **4**, 013233 (2022).

[68] J. Venkatraman, X. Xiao, R. G. Cortiñas, and M. H. Devoret, *On the static effective Lindbladian of the squeezed Kerr oscillator*, arXiv:2209.11193.

[69] X. Y. Jin, A. Kamal, A. P. Sears, T. Gudmundsen, D. Hover, J. Miloshi, R. Slattery, F. Yan, J. Yoder, T. P. Orlando, S. Gustavsson, and W. D. Oliver, *Thermal and residual excited-state population in a 3d transmon qubit*, Phys. Rev. Lett. **114**, 240501 (2015).

[70] J. M. Kreikebaum, A. Dove, W. Livingston, E. Kim, and I. Siddiqi, *Optimization of infrared and magnetic shielding of superconducting tin and Al coplanar microwave resonators*, Supercond. Sci. Technol. **29**, 104002 (2016).

[71] M. McEwen, L. Faoro, K. Arya, A. Dunsworth, T. Huang, S. Kim, B. Burkett, A. Fowler, F. Arute, J. C. Bardin *et al.*, *Resolving catastrophic error bursts from cosmic rays in large arrays of superconducting qubits*, Nat. Phys. **18**, 107 (2022).

[72] A. P. Vepsäläinen, A. H. Karamlou, J. L. Orrell, A. S. Dogra, B. Loer, F. Vasconcelos, D. K. Kim, A. J. Melville, B. M. Niedzielski, J. L. Yoder *et al.*, *Impact of ionizing radiation on superconducting qubit coherence*, Nature (London) **584**, 551 (2020).

[73] C. H. Liu, D. C. Harrison, S. Patel, C. D. Wilen, O. Rafferty, A. Shearrow, A. Ballard, V. Iaia, J. Ku, B. L. T. Plourde, and R. McDermott, *Quasiparticle poisoning of superconducting qubits from resonant absorption of pair-breaking photons*, Phys. Rev. Lett. **132**, 017001 (2024).

[74] C. Macklin, K. O'brien, D. Hover, M. Schwartz, V. Bolkhovsky, X. Zhang, W. Oliver, and I. Siddiqi, *A near–quantum-limited Josephson traveling-wave parametric amplifier*, Science **350**, 307 (2015).